Two computational studies of a flatback airfoil using non-zonal and embedded scale-resolving turbulence modelling approaches

Marian Fuchs[*] , Charles Mockett[†] , Felix Kramer[‡] and Thilo Knacke[§]
Upstream CFD GmbH, Bismarckstraße 10-12, D-10625, Berlin / Germany

Pascal Weihing[¶] , Timo Kühn[‖] and Henry Knobbe-Eschen[**]
WRD Wobben Research and Development GmbH, Teerhof 59, D-28199, Bremen / Germany

Michaela Herr[††] and Alexandre Suryadi[‡‡]
German Aerospace Center (DLR), Lilienthalplatz 7, D-38108, Braunschweig / Germany

The contribution presents results from two computational studies conducted by Upstream CFD and ENERCON, which aim to evaluate their respective CFD methodologies for the aerodynamics and aeroacoustics prediction of a flatback airfoil with 35% relative thickness. The CFD is validated against data from two comprehensive experimental campaigns conducted in the NWB facility operated by the German-Dutch Wind Tunnels Foundation (DNW), which include measurements of mean force coefficients, static and total pressure distributions in the wake region, unsteady surface pressures and farfield sound emission. In both numerical studies, scale-resolving approaches based on detached-eddy simulation are utilised, where a comparison is drawn between a purely non-zonal use of the model in which attached boundary layers are fully modelled via RANS and a zonal use with synthetic turbulence being injected into the boundary layers upstream of the trailing edge. First, the aerodynamic flow fields are analysed, showing good agreement with the reference measurements. Farfield noise is then predicted from solid and permeable Ffowcs-Williams and Hawkings surfaces, where both the dominant shedding tone as well as broadband levels compare well with microphone array data.

Nomenclature

a_0	=	reference speed of sound [m/s]
C_p	=	surface pressure coefficient [-]
$C_{p,s}$	=	static pressure coefficient [-]
$C_{p,t}$	=	total pressure coefficient [-]
c	=	chord length [m]
d_{TE}	=	trailing edge thickness [m]
k_{res}	=	resolved kinetic energy [m^2/s^2]
M_∞	=	freestream Mach number [-]
Re_c	=	Reynolds number based on chord length [-]
St	=	Strouhal number based on trailing edge thickness [-]
U_∞	=	freestream velocity [m/s]
U_0	=	reference velocity [m/s]
α	=	angle of attack [°]

[*]Senior CFD Consultant, email: marian.fuchs@upstream-cfd.com.

[†]Managing Director, email: charles.mockett@upstream-cfd.com.

[‡]Senior CFD Consultant, email: felix.kramer@upstream-cfd.com.

[§]Senior CFD Consultant, email: thilo.knacke@upstream-cfd.com.

[¶]Developer Wind Turbine Flow Simulation, email: pascal.weihing@enercon.de.

[‖]Head of Team Computational Fluid Dynamics, email: timo.kuehn@enercon.de.

[**]Aerodynamics Engineer, System Engineering Department, email: henry.knobbe-eschen@enercon.de.

[††]Head of Department Wind Energy, DLR Institute of Aerodynamics and Flow Technology, email: michaela.herr@dlr.de.

[‡‡]Research Engineer, DLR Institute of Aerodynamics and Flow Technology, Wind Energy, email: alexandre.suryadi@dlr.de.

δ	=	boundary layer thickness [m]
Δt	=	time step size [s]
$\Delta_{x/y/z}$	=	local grid spacing in the x/y/z-direction [m]
ζ	=	blending parameter of hybrid convection scheme [-]
θ	=	observer polar angle [°]
Ω	=	vorticity magnitude [1/s]
DES	=	detached-eddy simulation
DDES	=	delayed detached-eddy simulation
FWH	=	Ffowcs-Williams & Hawkings
IDDES	=	improved delayed detached-eddy simulation
LES	=	large-eddy simulation
PSD	=	power spectral density
RANS	=	Reynolds-averaged Navier-Stokes
SPL	=	sound pressure level
SRS	=	scale-resolving simulation
VSTG	=	volumetric turbulence synthetic generator
WMLES	=	wall-modelled large-eddy simulation

I. Introduction

The currently biggest challenge in the wind energy industry is the reduction of the levelised cost of electricity (LCOE). This means that the turbines have to progressively become more powerful and cost efficient. However, a simple geometric scaling of the turbines would lead to a disproportionate increase in the weight of the rotors and thus loads. To overcome this unfavourable circumstance, the blades must become slender and more elastic than in previous generations. In particular, airfoils with a high relative thickness need to be used to carry the loads in the inner part of the blades. Thicker airfoils with a blunt trailing edge, referred to as flatback airfoils, offer particularly good stiffness properties. Flatbacks also provide higher lift compared to sharp-edged airfoils with similar thickness due to a reduced pressure gradient on the suction side by shifting some of the pressure recovery to the airfoil's wake [1]. This also reduces the sensitivity to surface soiling effects, as it attenuates the risk of premature boundary layer separation [2]. The inherent advantages of flatbacks come to the expense of a higher overall drag due to an increased base drag at the trailing edge. In addition, significant low-frequent tonal noise is produced from the von Kármán-like vortex shedding as well as relevant broadband levels from the turbulent flow. The tonal component (blunt trailing edge noise = BTE) in particular can become a dominant noise source when flatback airfoils are installed at relatively outboard blade sections. Therefore, the aeroacoustic assessment of these airfoil types is important when evaluating the maximum allowed radial position for their integration. Since wind energy is seen as one of the key technologies for a transition to a greener, more sustainable industrial future, noise emissions can become a larger problem for the acceptance of wind energy as power plants move closer to urban areas.

For the future integration of flatback airfoils into new blade designs to be successful, numerical design tools must be able to accurately predict both the aerodynamic performance as well as radiated farfield noise. Unfortunately, the characteristic flow features exhibited by thick airfoils with blunt trailing edges are out of reach to predict for traditional RANS approaches. In this contribution, we therefore want to explore high-fidelity scale-resolving approaches, in particular different variants of detached-eddy simulation (DES), for this task. The DES method belongs to the class of hybrid RANS-LES models and has already shown promising potential for such flow types, e.g. in the studies of Stone et al. [3] and Papadakis & Manolesos [4]. The airfoil investigated in this work is a proprietary geometry of ENERCON, which exhibits a maximum thickness-to-chord ratio of 35% and a trailing edge thickness of ∼ 5.2% chord. Within the framework of the German-funded research project IndiAnaWind (2019-2022), two extensive measurement campaigns have been conducted in the DNW-NWB facility (located in Braunschweig / Germany) operated by the German-Dutch Wind Tunnels Foundation (DNW), from which high-quality aerodynamic and aeroacoustic reference data has been made available for CFD validation to the authors (see section II). The goal of this work is to evaluate the current computational methodologies of Upstream CFD and ENERCON (i.e. flow solvers, numerics, meshing, turbulence modelling approaches, see section III) for this application type as well as to identified potential issues which need to be addressed in the future. The simulations using the ENERCON methodology are conducted by Wobben Research and Development GmbH (WRD), the external research and method development department of ENERCON. A particular focus is placed on the scale-resolving turbulence modelling approach, where two principle operation modes

are compared: a) a traditional non-zonal usage of DES, where the model autonomously decides in which parts of the domain to apply either RANS or LES and b) a zonal / embedded usage of DES, where the user explicitly prescribes a location at which resolved turbulence is injected into the flow field. The essential difference between both operation modes constitutes the modelling that is applied inside the attached boundary layers upstream of the trailing edge, where the non-zonal mode enforces full RANS treatment whereas the zonal mode leads to a wall-modelled LES (WMLES) type of simulation in this region.

II. Experimental campaigns

The NWB (*Niedergeschwindigkeits-Windkanal Braunschweig*) located on the premises of DLR in Braunschweig / Germany is a closed-circuit low-speed wind tunnel of the atmospheric type, which underwent substantial refurbishment from 2009 to 2010 to allow for very accurate aeroacoustic measurements in addition to its already established high aerodynamic qualities [5]. Two successive experimental campaigns were conducted in 2020 with the aim of obtaining a consistent evaluation of the aerodynamic and aeroacoustic properties of different wind turbine blades as well as performance enhancing add-ons (i.e. vortex generators - VGs). Two different test sections were utilised for this purpose, which are shown in figure 1.

Campaign in closed test section (09/20)   **Campaign in open test section (11/20)**

Fig. 1   Images of the two different measurement campaigns conducted in the NWB wind tunnel within the framework of the German-funded IndiAnaWind project.

First, aerodynamical measurements were conducted in a closed test section with a cross-sectional area of 3.25 m × 2.8 m and a length of 8.0 m. The airfoil mock-up exhibited a chord length of $c = 0.7$ m and was manufactured and equipped by Leichtwerk AG*. Two different variants of the same proprietary profile from ENERCON were investigated, which both featured a maximum thickness-to-chord ratio of 35%. One variant that is the main focus of the numerical investigation in this paper featured a blunt trailing edge with a thickness of $d_{TE} \sim 0.052\ c$, and the other variant featured a sharp trailing edge. The aerodynamic performance of the profiles was assessed at Reynolds numbers of $Re_c = 2 \times 10^6$ and 3.5×10^6 (based on the chord length) and for configurations with and without equipped vortex generators. The data set acquired in this test contains both mean flow as well as unsteady quantities. Mean force coefficients and moments were measured over a range of different angles of attack, i.e. $-4° \leq \alpha \leq 22°$, to establish the overall aerodynamic performance of each airfoil configuration, the separation behaviour at maximum lift as well as potential hysteresis effects. As shown in figure 2, the experimental mock-up was equipped with two rows of static pressure taps (with approx. 90 taps in each row), which are located at 22% and 62% span width measured from the bottom wall of the closed test section. To obtain more insight into the unsteady flow behaviour and potential aeroacoustic sources, a number of high-resolution Fos4x fiber optic sensors were installed on both airfoil sides at streamwise locations of $x/c = 0.5$, 0.86, 0.91 and 0.935 (see figure 2). In addition, mean static / total pressures in the wake region were measured via transverse rakes. All airfoils were run in essentially two transition configurations in both campaigns, i.e. a) a clean profile which

*https://www.leichtwerk.de/

3

allows free transition and b) a profile with fixed transition locations on the pressure and suction sides. The manual tripping was hereby achieved via the application of two layers of tape (i.e. a layer of 0.008 mm Kapton and a layer of 0.255 mm ZZ-shaped tape), which were glued on at 5% chord on the suction and 10% chord on the pressure side of the airfoil (shown in figure 3). This allows for a cleaner validation with the CFD, and significantly reduces uncertainties with regard to the transition modelling in the simulations.

Static pressure taps   **Fos4x sensors**
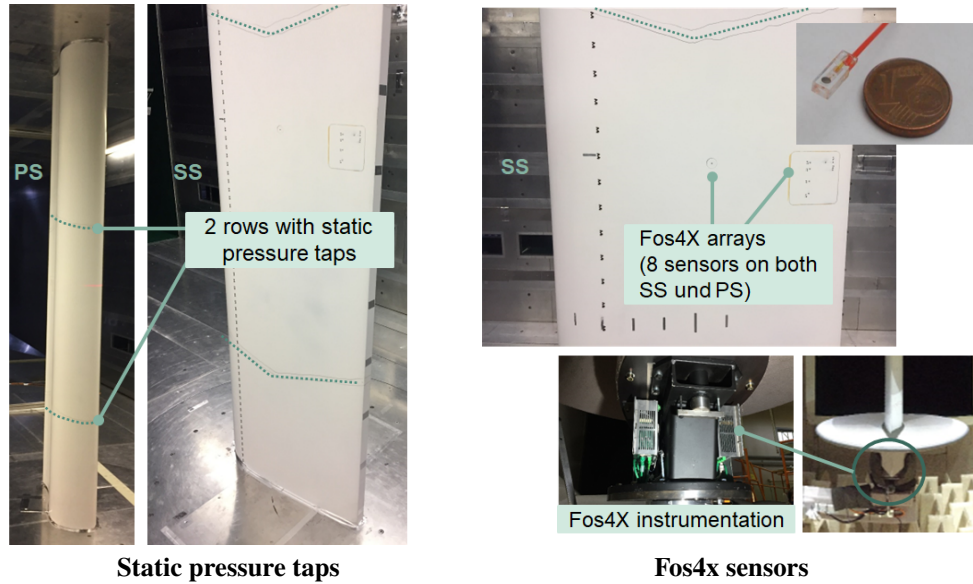
Fig. 2   Images of installed measurement instrumentation in airfoil mock-up.
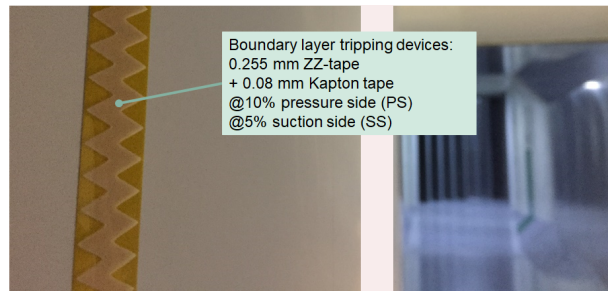

Fig. 3   Tripping device installed on the airfoil mock-up used in both experimental campaigns.

The aerodynamic campaign was then complemented by a second campaign in an open-jet test section (see figure 4), where the same retrofitted mock-up with a span width of 2.1 m (i.e. aspect ratio of 3) was placed in an anechoic plenum of size 14 m × 16 m × 8 m, which provides 99% acoustic damping in an ISO 3745 certified frequency range of 100 Hz to 40 kHz. Since the same instrumented mock-up was used as in the first campaign, consistent surface data could be acquired in both campaigns (i.e. static surface pressure distributions and unsteady surface pressure spectra). However, no wake rakes were installed in the aeroacoustical campaign for practical reasons. Measurements were again conducted for different airfoils / VG configurations and at different flow speeds of 40, 55, 70 and 80 m/s, which correspond to Reynolds numbers of $Re_c = \{1.7, 2.4, 3.1, 3.5\} \times 10^6$. Relative to the closed section, the span width had to be shortened from 2.8 m to 2.1 m to keep the open-jet free shear layers outside of the two end plates used in the acoustic setup. Accordingly, the static pressure taps were positioned to 12.6% span width measured from the bottom circular plate and at 34% span width from the top plate.

Aeroacoustic farfield data were collected via different measuring devices, which are shown in figure 4. First, a microphone array consisting of 140 microphones and with an outer diameter of 2.8 m was mounted towards the airfoil's suction side. The horizontal distance of the microphone array's plane to the center plane of the wind tunnel is 2.67 m. From the microphone array measurements, acoustic source maps were deduced via the CLEAN-SC procedure [6], where diagonal removal of the cross-spectral matrix as well as a 2D Amiet shear layer correction were applied. The deduced area covers both the leading and trailing edges of the wind tunnel model and is 1 m wide along the spanwise direction (centered around the mid-span line of the model). From the acoustic source maps, a farfield spectrum is also produced via power integration. Spectral analysis was performed using the averaged periodogram method with a rectangular window and 0% overlap between each periodogram.
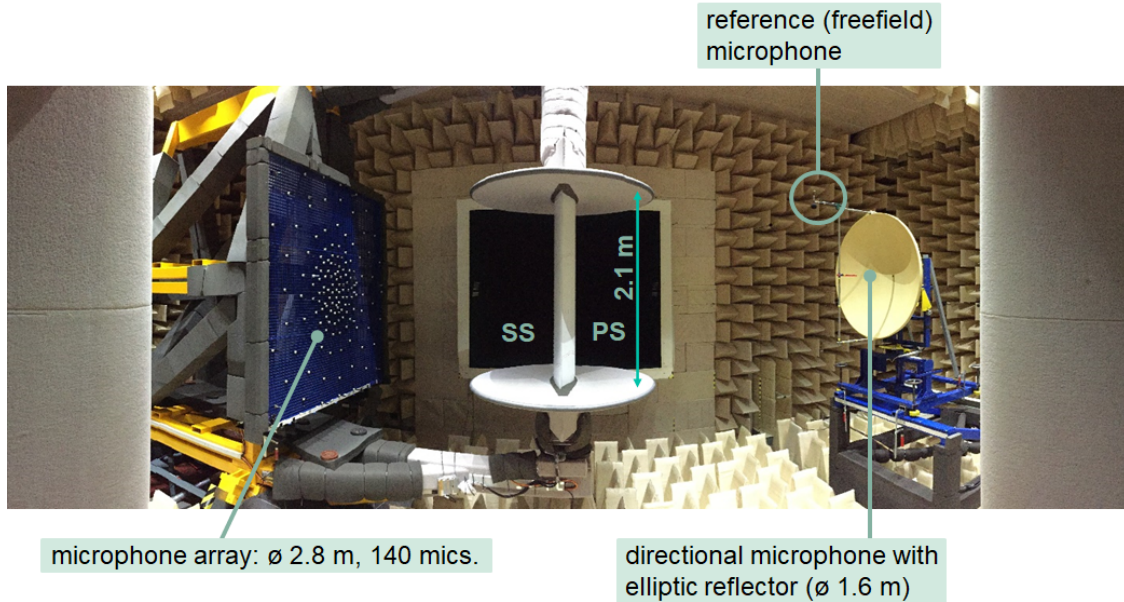

Fig. 4   Aeroacoustic measurement instrumentation during campaign in open test section of NWB wind tunnel.

In addition to the microphone array, a directional microphone (1/4" B&K 4136) with an elliptic reflector (diameter of 1.6 m) was mounted facing the airfoil's pressure side. Above the reflector, a reference microphone (1/2" G.R.A.S. 40AC with foam ball) was installed. The horizontal distances between the centre plane of the wind tunnel to the directional and reference microphones are 3.34 m and 2.71 m, respectively. Measured data from the directional microphone were corrected for background noise and the system response function (including sound refraction and scattering through the open-jet shear layer) according to the method of Schlinker [7]. Due to the insensitivity of the directional microphone to the source distance, the source-to-sensor distance was kept constant and not recalculated for every angle of attack [8]. Source convection was accounted for by positioning both the directional and reference microphones downstream of the airfoil trailing edge at velocity-dependent distances that correspond to the best representation of the sound source position, i.e. a local sound pressure level maximum along the streamwise axis. The reference microphone signals were corrected for background noise, atmospheric and convective damping as well as the microphone's off-axis response function. The apparent distance from the reference microphone to the convected sound source (i.e. trailing-edge noise source) was also corrected for. Because the reference microphone is attached to the directional microphone, it can be confirmed that the apparent sound source is in front of the directional microphone's reflector within ±1.5°. The directional and reference microphone signals were analysed using the averaged periodogram method with a Hanning window and 50% overlap between each periodogram.

All resulting narrowband spectra from the three measurement devices exhibit a frequency resolution of $\Delta f = 6.25$ Hz, and were sampled at a rate of 102.4 kHz over a time period of 30 s. Levels were scaled to an observer at a distance of 1 m away from the sound source via $-10\log_{10}(r^2/1)$, where r is the distance of each sensing element to the apparent position

of the sound source. The sound levels from the microphone array and the directional microphone are additionally scaled for a line source of 1 m span. In contrast, the levels of the reference microphone spectrum were not corrected for span width, since the data contains all sound sources inside the wind tunnel, including spurious contributions from tunnel background noise, the model end plates as well as the struts. Because of their respective positions, the spectra from the directional and reference microphones represent levels as observed by an observer facing the pressure side of the airfoil, and the spectra from the microphone array for an observer facing the suction side.

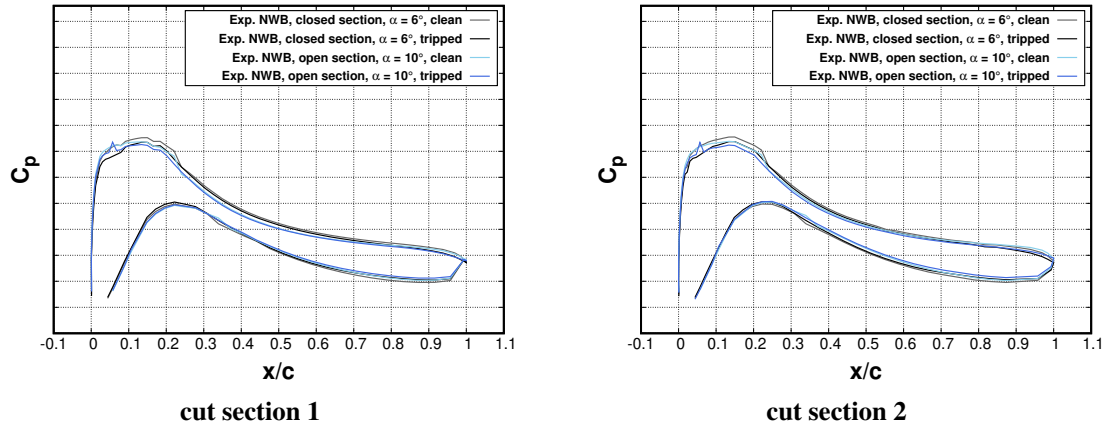cut section 1   cut section 2

Fig. 5   Comparison of surface pressure distributions from closed and open wind tunnel campaigns at different geometrical angles of attack. Flatback airfoil without VGs, both with and without applied boundary layer tripping. Closed section measurements at $Re_c = 3.5 \times 10^6$ and $M_\infty = 0.228$, open section measurements at $Re_c = 3.1 \times 10^6$ and $M_\infty = 0.201$.
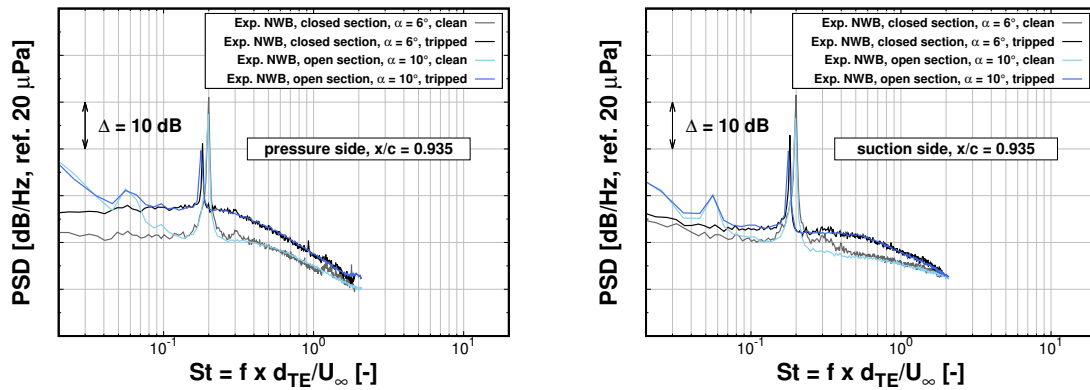

Fig. 6   Comparison of surface pressure spectra from closed and open wind tunnel campaigns at different geometrical angles of attack. Flatback airfoil without VGs, both with and without applied boundary layer tripping. Closed section measurements at $Re_c = 3.5 \times 10^6$ and $M_\infty = 0.228$, open section measurements at $Re_c = 3.1 \times 10^6$ and $M_\infty = 0.201$.

In the aeroacoustic campaign, aerodynamic polars were first recorded to identify angles of attack for which surface pressure contributions can be matched between closed and open wind tunnel tests. This proved to be challenging, since flow separation occurred at much lower effective angles of attack in the open jet rig, so that pressure distributions could not be matched between both tests for large angles of attack close to maximum lift. However, for the flatback airfoil with 35% relative thickness investigated in this work, a sufficient aerodynamic performance comparability could be achieved between the runs at $\alpha = 6°$ in the closed test section and $\alpha = 10°$ in the open test section, as is

demonstrated by cross-plotting the measured surface pressure distributions in the two cut sections from both experiments in figure 5. Slightly lower lift is produced in the open test section, whereby the trends between the clean and tripped configurations seem to be consistent. A somewhat stronger flow acceleration around the airfoil leading edge is present in the measurements without tripping devices, and the offset in C_p seen between clean and tripped configurations is consistent in both campaigns.

In figure 7, farfield spectra measured a) via the reference microphone and b) post-processed from the microphone array data are compared for different flow velocities and between the tripped and clean configurations. It can be seen that the spectra seem to collapse when re-scaled for Mach number with a scaling exponent of 5. Likewise, scaling of the frequency axis via the Strouhal number seems to be appropriate and leads to a collapse of the dominant shedding tones. The Strouhal number (based on the trailing edge thickness) at which the base tone occurs is slightly shifted downwards from $St \approx 0.20$ for the clean configuration to $St \approx 0.18$ for the tripped configuration. The tripping also reduces the sound level of the dominant tone by 6 to 10 dB. The first and second harmonics are especially pronounced in the array measurements for the clean configuration, and are significantly reduced when the boundary layers are tripped. Broadband levels for the reference microphone are generally overestimated and are not representative for the clean airfoil, since the signals include additional noise sources from the test rig (e.g. spurious noise from model support struts), and are hence not used for validation in this work. For the microphone array spectra, some processing artefacts (i.e. kinks in the sound pressure levels) can be seen, which are associated with the applied CLEAN-SC procedure. The method removes all noise sources outside of the area of interest, which, combined with the rectangular window used in the cross-spectra calculation, produces the kinks in the microphone array spectra. In general, the Mach number and frequency scaling of the farfield spectra is a mix of the level scaling of a turbulent boundary layer generating trailing-edge noise and the frequency scaling of the blunt trailing-edge vortex-shedding noise [9]. With regard to the tones generated by the vortex shedding, we observe tonal levels that scale similar to trailing-edge noise, but are inconsistent with the 5.5 exponent presented in Brooks et al. [9]. This is a mixture of two mechanisms: a compact dipole due to the vortex shedding noise and a non-compact dipole source from edge noise. Here, the tones appear to be generated mainly by the edge mechanism. The frequency exponent of -2 seen in the microphone array spectra is also consistent with the farfield spectrum of turbulent boundary layers generated via trailing edge noise [10]. Unfortunately, the directional microphone data was not yet available at the time of the publication, so that no further analysis is presented in this paper for this data set.

farfield sound - reference microphone
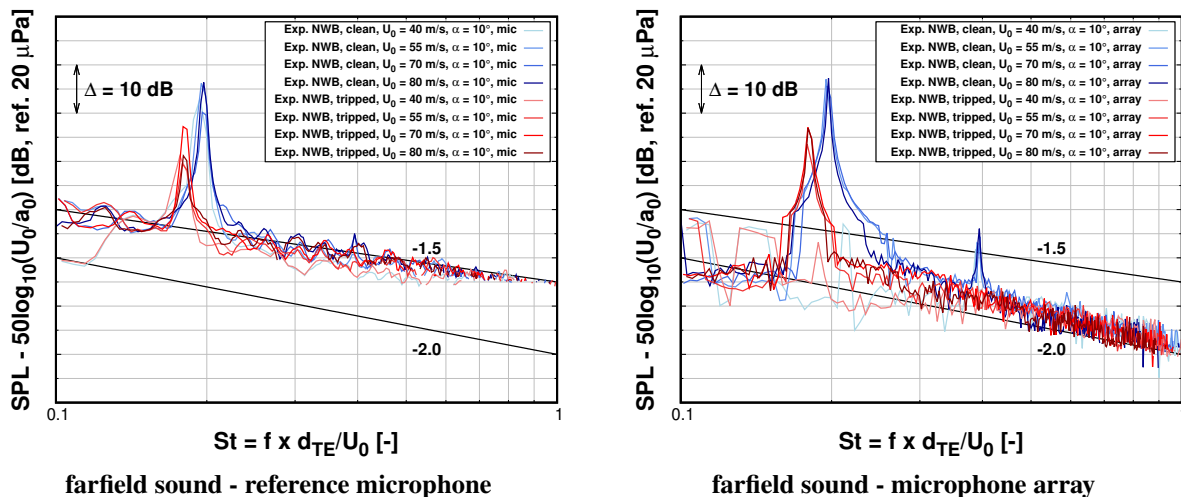
farfield sound - microphone array

Fig. 7   Comparison of farfield sound spectra measured via reference microphone on pressure side and microphone array on suction side. Flatback airfoil without VGs, both with and without applied boundary layer tripping. Spectra from microphone array are normalised to a span width of 1 m **and an observer distance of** 1 m**.**

III. Computational approaches

In this section, the two computational approaches utilised in this study by Upstream CFD and WRD are detailed. Both approaches are based on scale-resolving simulations to capture the acoustic sources in the near field, followed by a subsequent post-processing step in which the farfield sound is extrapolated via the Ffowcs Williams-Hawkings equation (FWH) from collected unsteady source data. Solver and turbulence modelling details are described in the following two sub-sections III.A & III.B, whereas details with regard to the aeroacoustic post-processing are given in section IV.C.

A. Computational approach of Upstream CFD

Upstream CFD employs an enhanced version of the pressure-based solver that comes as part of the open source software package OpenFOAM[†] and solves the fully compressible Navier-Stokes equations. The solver can handle unstructured grids with arbitrary cell shapes (e.g. no limitation for number of faces when using polyhedral cells) and is based on finite volume discretisation. Coupling of velocity and pressure in a collocated arrangement is achieved via a transient SIMPLE algorithm using multiple sub-iterations per time step, where odd-even decoupling is prevented by using a Rhie & Chow type interpolation. The employed specific Rhie & Chow formulation was carefully adapted and validated to be compatible with aeroacoustics simulations in previous work of Knacke [11], and exhibits low levels of spurious noise, which is a common problem for pressure-based solvers employed to low Mach number aeroacoustics. To guarantee adequate treatment of resolved turbulent structures in the LES region of the domain, spatial and temporal discretisation schemes that exhibit low levels of numerical dissipation are applied. Time integration is performed using an implicit second order accurate Euler scheme. The convective fluxes are discretised using the hybrid blending approach of Travin et al. [12] The approach blends locally between a numerically robust upwind-biased scheme in the irrotational region and a low dissipative 2nd order accurate central differencing scheme (CDS) in regions of resolved turbulence. During the study, different settings of the hybrid blending scheme were investigated with the aim of reducing spurious noise in the near field / wake region, which are discussed in more detail in section V.D.

To enable an accurate prediction of both tonal and broadband noise, a scale-resolving turbulence modelling approach is pursued by Upstream CFD. This allows the direct simulation of acoustic sources in the near field. In this context, two different methodologies are compared (see figure 8), which are both based on a DES-type hybrid RANS-LES model that offers a good compromise between computational efficiency in attached boundary layers at high Reynolds numbers and reliable LES resolution in separation regions. The applied DES model is the σ-DDES approach of Mockett & Fuchs [13] [14], which offers an accelerated transition from RANS to LES in separated shear layers, a problem often encountered for standard DES methods and termed "grey area" (GA). First, the model is applied in a non-zonal manner, which is the natural operation mode of DES. The model hereby autonomously decides where to apply either RANS or LES mode based on a length scale comparison and the activity of a model-specific shielding function, which aims to prevent the activation of the LES mode inside of attached boundary layers. This effectively leads to a situation where the attached flow on both sides of the airfoil is modelled via RANS, and LES mode is only applied in the wake region downstream of the trailing edge, as illustrated in figure 8. In this study, the behaviour of the shielding function is further assessed, where the standard shielding function used in the established delayed DES (DDES) model of Spalart et al. [15] is compared to an improved formulation which has been published more recently by Deck & Renard [16] (see section V.A).

A second methodology is explored, whereby synthetic turbulence is injected inside the attached boundary layers in a region upstream of the trailing edge, for which the volumetric synthetic turbulence generator (VSTG) method of Shur et al. [17] is used. This methodology is referred to as zonal or embedded, since the user has to explicitly prescribed where to inject the turbulence and hence where to force the switch from RANS to LES mode (i.e. where to embed the LES mode). Unlike for 2D synthetic turbulence generator methods which typically inject the resolved eddies at predefined interface planes, the selected VSTG method allows for an easier integration into simulations with complex geometries as well as a more flexible placement of the synthetic turbulence zone. Furthermore, the injection of turbulent structures via volumetric source terms in the momentum equations allows for a more gradual generation of resolved content, which is generally more acoustically friendly and generates less spurious noise [17]. On the airfoil parts between VSTG zone and trailing edge, the model switches to a scale-resolving mode instead of pure RANS, which can be classified as a wall-modelled LES (WMLES) type of simulation. The WMLES mode allows to resolve the outer part of the boundary layer via LES, whereas the more computationally expensive near-wall part is still modelled via RANS. In [18], it was demonstrated that the σ-DDES variant is capable of being applied in a WMLES-type manner, if

---

[†]https://www.openfoam.com/

sufficiently resolved content is injected in the boundary layer region, and is hence used for the zonal simulations of Upstream CFD to maintain a comparable LES mode operation relative to the non-zonal simulations. In both turbulence modelling methodologies, the Spalart-Allmaras model is used as RANS background model for the DES variant.
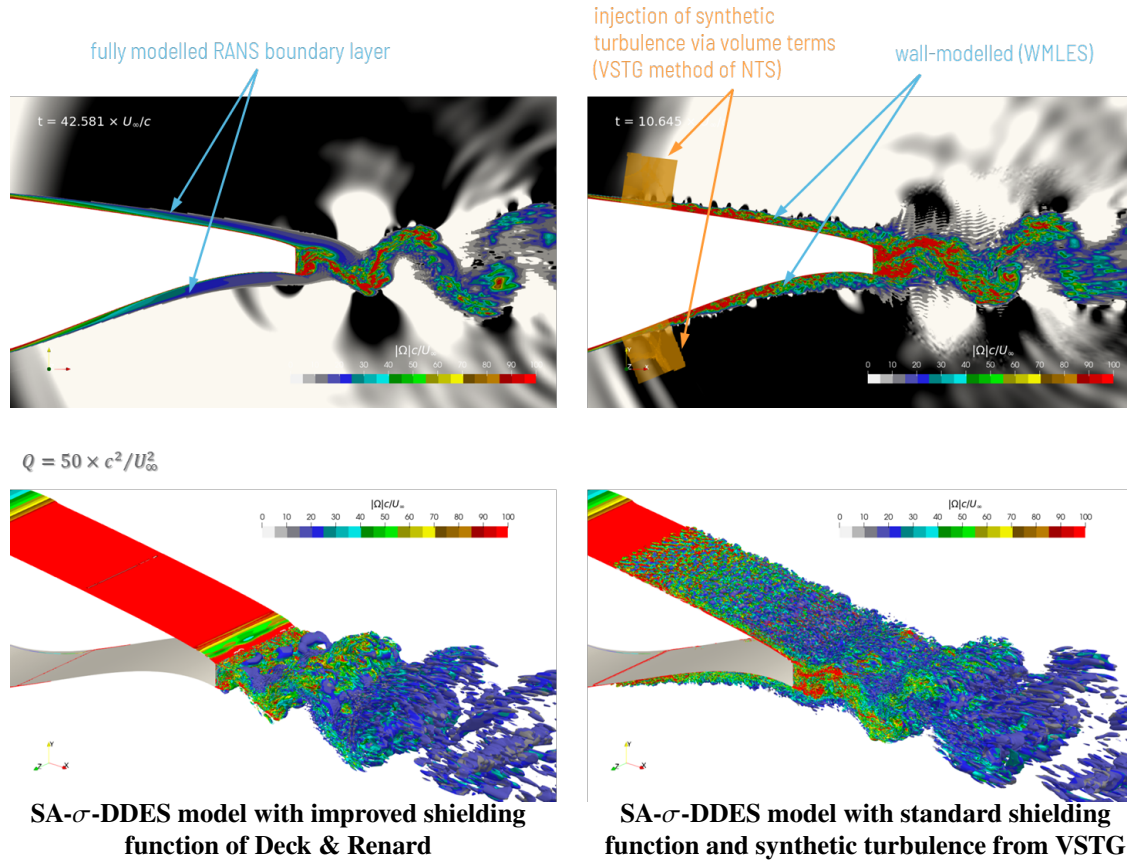

SA-σ-DDES model with improved shielding function of Deck & Renard

SA-σ-DDES model with standard shielding function and synthetic turbulence from VSTG

Fig. 8   Overview about turbulence modelling approaches applied by Upstream CFD.

B. Computational approach of ENERCON

WRD employs the block-structured density-based FLOWer code [19] in this study, which has been continuously developed at the DLR, the Institute of Aerodynamics and Gas Dynamics (IAG) at the University of Stuttgart and other collaborating academic institutions since the late 1990s. It solves the fully compressible Navier-Stokes equations using the finite volume approach, where the discretisation of the Euler fluxes is based on central differences with artificial dissipation [20] using a value of $k4 = 1/256$. Viscous fluxes are also discretised using central differences. For time integration, the dual-time stepping approach of Jameson [21] is employed.

The turbulence modelling methodology used is equivalent to the zonal approach applied in the Upstream CFD simulations. The same VSTG method is utilised to inject resolved turbulence in the boundary layers upstream of the trailing edge. In contrast to the Upstream CFD approach, WRD applies the improved delayed DES (IDDES) variant based on the k-ω SST model in their simulations, which is a DES variant specifically designed to enable a WMLES-type operation [22]. An instantaneous snapshot of the productive simulation showing resolved turbulent structures is depicted in figure 9.
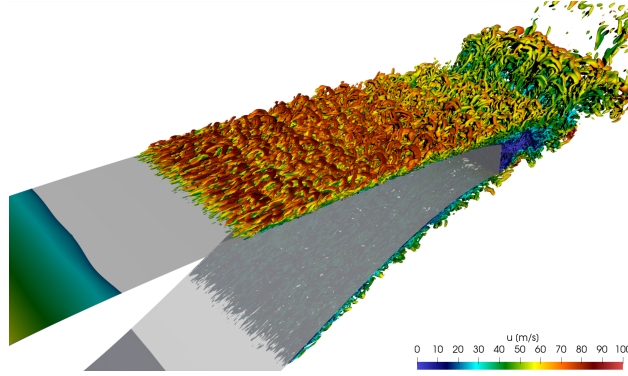
Fig. 9 Turbulence modelling approach applied by WRD: SST-IDDES model and synthetic turbulence from VSTG method.

IV. Test case setup

A. Geometry & case parameters

The flatback airfoil investigated in this study is a proprietary geometry of ENERCON GmbH, and can for this reason only be partially disclosed in this publication. It exhibits a maximum thickness-to-chord ratio of 35% and a trailing edge width of $d_{\mathrm{TE}} \sim 0.052\ c$. The simulations of both partners were conducted at slightly different flow conditions, which are listed in table 1.

Table 1   Flow conditions in experimental campaigns and CFD simulations.

	Exp. NWB (closed test section)	Exp. NWB (open test section)	CFD (WRD)	CFD (UCFD)
Reynolds number, Re_c	3.5×10^6	3.1×10^6	3.5×10^6	3.5×10^6
Freestream Mach number, M_∞	0.228	0.201	0.201	0.219
Freestream velocity, U_∞	79.4 m/s	70.1 m/s	70.0 m/s	74.5 m/s
Geometrical angle-of-attack, α	6°	10°	6°	6°
Ambient pressure, p_∞	100479 Pa	100755 Pa	114709 Pa	101325 Pa
Ambient temperature, T_∞	300.9 K	301.7 K	301.7 K	288.15 K
Ambient density, ρ_∞	1.165 kg/m^3	1.160 kg/m^3	1.324 kg/m^3	1.225 kg/m^3

Upstream CFD developed their case setup prior to both experimental campaigns and conducted their simulations as a blind study. Ahead of the first test in the closed section wind tunnel, the estimated flow conditions for the experimental reference data set were $Re_c = 3.5 \times 10^6$ and $M_\infty = 0.219$, so these values were used in the CFD setup of Upstream CFD along with ISA standard conditions for the thermodynamic quantities. Ultimately, slightly different flow conditions were present in both experimental campaigns, where the Mach number in the closed section measurements was $\sim 4\%$ higher than in the CFD setup of UCFD. From the two experimental data sets of the aeroacoustical test measured at $Re_c = 3.1\ \&\ 3.5 \times 10^6$ (which corresponds to $M_\infty = 0.201\ \&\ 0.228$), aerodynamical quantities were only available for cross-comparison with the CFD data for the first set at the time of the publication. WRD generated their CFD setup after the completion of all wind tunnel tests, and opted to emulate the conditions of the acoustics measurements at $M_\infty = 0.201$. However, WRD prescribed a Reynolds number that is equivalent to the UCFD setup. The Mach number influence on the farfield sound levels was corrected via appropriate scaling laws, as detailed in section IV.C. Both CFD setups used freefield conditions, where the farfield boundary patches were placed sufficiently far away from the airfoil to have negligible impact on the computed aerodynamics and aeroacoustics (see section IV.B). A modest angle of attack of $\alpha = 6°$ was investigated in the CFD, for which comparable aerodynamical behaviour (i.e. generated lift and surface

pressure distribution) could be achieved in both experimental campaigns (see figure 5). The geometrical angle of attack is hereby equivalent to the angle of attack used in the closed section test, but significantly lower than the angle of attack required in the aeroacoustical test with open jet configuration (i.e. $\alpha = 10°$).

B. Computational grids & CFD setup

Very similar meshing strategies have been applied by both partners, where relevant statistics of all computational grids are listed in table 2. Both UCFD and WRD used a block-structured meshing approach to guarantee best possible cell topology and hence low numerical errors for reliable aeroacoustics prediction. A structured meshing approach also allows to fully control the cell-to-cell stretching rates by the user and avoid strong cell jumps, which can cause spurious noise if resolved turbulence is convected over them. Both partners conducted 2.5D simulations, i.e. a spanwise extrusion of the 2D profile, where periodic boundary conditions with fully matching grids were applied in the spanwise direction (z). The spanwise domain width was set to $L_{\text{span}} = L_z = 0.25c$. This decision was based on findings of Metzinger et al. [23], who concluded from their study that a domain width of $L_{\text{span}} \sim 5 \times d_{\text{TE}}$ should suffice for the pressure to fully decorrelate in the spanwise direction for low angles of attack and flatback profiles where separation mainly emanates from the blunt trailing edge. This is anticipated to be the case for the simulated angle of attack $\alpha = 6°$ in this study. For larger angles of attack however, a larger spanwise domain extent would become necessary, since the turbulent structures separating from the pressure side of the airfoil generally exhibit larger correlation lengths [24]. In accordance to the procedure used in both experimental campaigns, user-defined tripping locations were applied in both CFD setups to fix the laminar-to-turbulent transition points at 5% chord on the suction side and 10% chord on the pressure side by switching off the turbulence production terms in the transport equations upstream of these locations.

Table 2 **Grid statistics and simulation settings for all partner simulations. Local boundary layer thickness δ was deduced from steady-state RANS simulation of Upstream CFD.**

	non-zonal grid UCFD	zonal grid UCFD	zonal grid WRD
Domain span width, L_{span}	0.25c	0.25c	0.25c
Total cell count	24.4×10^6	27.2×10^6	96×10^6
Δ_x in WMLES region, $0.5 \leq x/c \leq 1.0$	$0.001c - 0.008c$	$0.001c - 0.002c$	$0.0011c$
Δ_z in WMLES region, $0.5 \leq x/c \leq 1.0$	$0.00195c$	$0.00195c$	$0.00065c$
Δ_z in wake focus region, $1.0 \leq x/c \leq 1.2$	$0.00195c$	$0.00195c$	$0.00065c$
Δ_z in wake departure region, $1.2 \leq x/c \leq 1.7$	$0.00195c$	$0.00195c$	$0.0013c$
$\delta/\Delta_x, \delta/\Delta_z$ at $x/c = 0.6$	3, 13	13, 13	23, 39
$\delta/\Delta_x, \delta/\Delta_z$ at $x/c = 0.9$	15, 13	21, 22	35, 66
Wall-normal cell stretching ratio in BL, r_{BL}	1.15	1.15	1.06
Cell stretching ratios in near wake, r_x, r_y	1.02, 1.02	1.02, 1.02	1.01, 1.05
Points across trailing edge in the y-direction	212	212	113
Time step size, $\Delta t \times U_\infty/c$	0.001	0.001	0.001
Length of initial transient, $T_{\text{ini}} \times U_\infty/c$	10.7	10.7	8.0
Length of statistical sampling, $T_{\text{stat}} \times U_\infty/c$	31.9	31.9	24.0
Write interval for FW-H data	every 5th Δt	every 5th Δt	every 2nd Δt

In figure 10, different views of the two computational grids employed by Upstream CFD in this study are presented. The blocking structure used in the computational grid of WRD for regions featuring resolved turbulence is shown in figure 11, along with selected statistics about the points distribution in each block. Slightly different grids were employed in the non-zonal and zonal simulations of UCFD, where additional refinement in the streamwise (x) and spanwise (z) directions was added on the suction and pressure sides of the airfoil for the "zonal grid" (between $0.5 \leq x/c \leq 1.0$, where the coordinate system origin is located at the airfoil leading edge). This was necessary to adhere to specific best practice meshing guidelines for performing sufficiently resolved WMLES, since the model switches to scale-resolving mode inside and downstream of the VSTG region. For the "non-zonal" grid however, the turbulence model is expected

to be still in (2D) RANS mode up until close to the trailing edge, so that roughly 3M grid points could be saved be removing the additional boundary layer refinement in this case. For all grids, the domain features a C-shape topology, where the farfield boundaries were placed $100c$ away from the airfoil to minimise their effect on the aerodynamics and acoustic wave propagation. In the vicinity of the airfoil and the wake region, low cell-to-cell stretching ratios are applied for all grids to avoid a too rapid stretching of resolved vortices. The UCFD grids exhibit a cell-to-cell stretching ratio of 2% in the near wake, whilst the WRD grid features ratios of 1% and 5% in the streamwise and lateral (y) directions, respectively. To save grid points in the inviscid / farfield region, 2:1 cell jumps were used by UCFD and carefully placed outside of the turbulent regions (the coarse cells at the 2:1 interface are treated as polyhedral cells in the OpenFOAM code). Most of the grid jump locations are radially placed, except for the far downstream part of the domain where one hanging nodes interface was placed in the streamwise direction. A variable distribution of grid points was also applied in the spanwise direction (see figure 10). In the turbulent wake region, a number of $N_z = 128$ spanwise points was used to achieve a nearly isotropic resolution in the near-wake (so that Δ_z corresponds roughly to Δ_x and Δ_z), whereas only $N_z = 16$ points were used outside in the farfield region. The reduction of cell count associated to the introduction of the 2:1 coarsening is about a factor 2 relative to the base grid without grid jumps. A similar concept was used in the meshing approach of WRD. Here, 2:1 cells jumps in the form of true hanging nodes were applied in the spanwise direction, where the grid interface was placed in the near wake region at $x/c \approx 1.2$. In contrast to the UCFD grids, no hanging nodes were implemented in the x/y-plane in the WRD grid, so that some of the near field refinement leads to partially excessive resolution in the farfield region. It is planned to implement further 2:1 hanging node interfaces in a future version of the meshing tool chain.
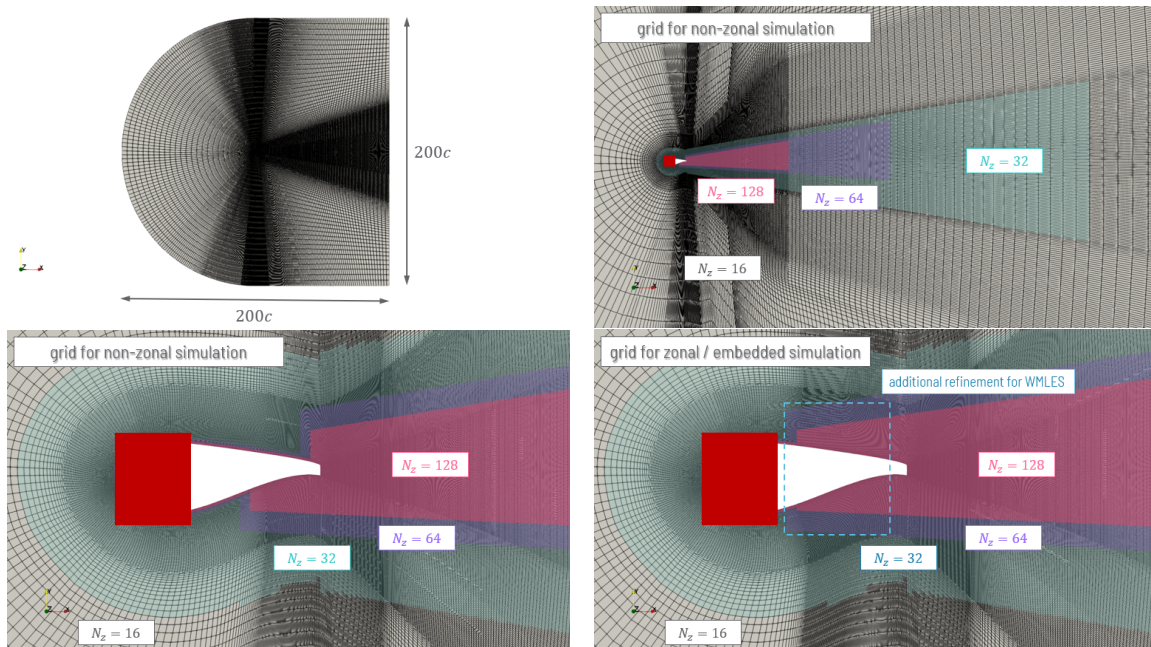

Fig. 10   Overview about meshing strategy of Upstream CFD.

With regard to the boundary layer resolution in the RANS region, established best practice guidelines for external aerodynamics are followed. The first wall-normal spacing was adjusted via a precursor RANS by both partners to achieve $y^+_{max} \sim 1$ in the first cell centre. The wall-normal stretching ratio of the UCFD grids is $r \sim 1.15$, WRD used a somewhat lower growth rate of $r \sim 1.06$. To determine the grid resolution in the streamwise (Δx) and spanwise (Δz) directions inside the WMLES region for the zonal simulation approach, best practice values are commonly measured / assessed in points per boundary layer thickness δ, where values of $\delta/\Delta x = 10$ and $\delta/\Delta z = 20$ are cited by e.g. Menter [25]. For the wall-normal direction, a number of $N_y \sim 30 - 40$ points per boundary layer thickness is an established value. This means that WMLES becomes increasingly expensive for thin boundary layers, since the local cell spacing then has to be adapted accordingly. For airfoil aerodynamics, this implies that especially the region around the airfoil nose is

12

computationally very expensive if resolved via WMLES. Therefore, only the downstream part of both airfoil surfaces is equipped with a suitable WMLES resolution for the flatback simulations in this study. To allow for a more quantitative analysis, the local boundary layer thickness on both suction and pressure sides has been extracted from a precursor RANS, and is plotted in figure 12. On the suction side at $x/c = 0.6$, the local boundary layer thickness is approximately $0.3c$. For the zonal WMLES grid of UCFD, this results in a resolution of $\delta/\Delta x \sim 13$, $N_y \sim 54$ and $\delta/\Delta z \sim 13$ (thus a slightly lower spanwise resolution compared to the cited best practice). Due to the further boundary layer growth towards the trailing edge, these values then rise to $\delta/\Delta x \sim 21$, $N_y \sim 58$ and $\delta/\Delta z \sim 22$ at $x/c = 0.9$, which should be adequate to perform reliable WMLES. However, much more aggressive grid refinement was applied by WRD for their grid in the WMLES region, where the local grid resolution featured at $x/c = 0.6$ is $\delta/\Delta x \sim 23$, $N_y > 100$ and $\delta/\Delta z \sim 39$, respectively. This constitutes a refinement by a factor of 2 in the streamwise and a factor of 3 in the spanwise direction relative to the zonal grid of UCFD. In addition, a much larger number of points is clustered in the wall-normal direction due to the low cell-to-cell stretching ratio of 6% applied by WRD. Subsequently, the total cell count is roughly 3.5 times higher for the WRD grid, which exhibits approximately 96M cells.
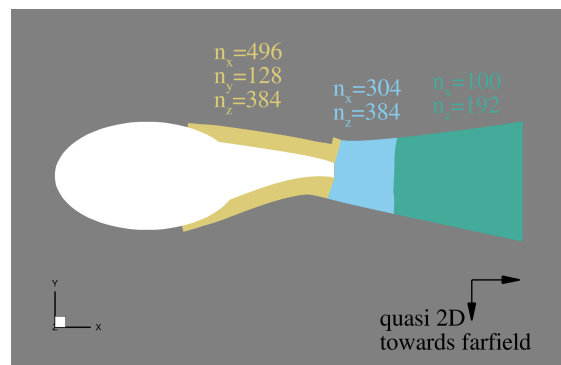

Fig. 11   Overview about block structure and point distribution in the boundary layer and near wake regions for the computational grid of WRD.
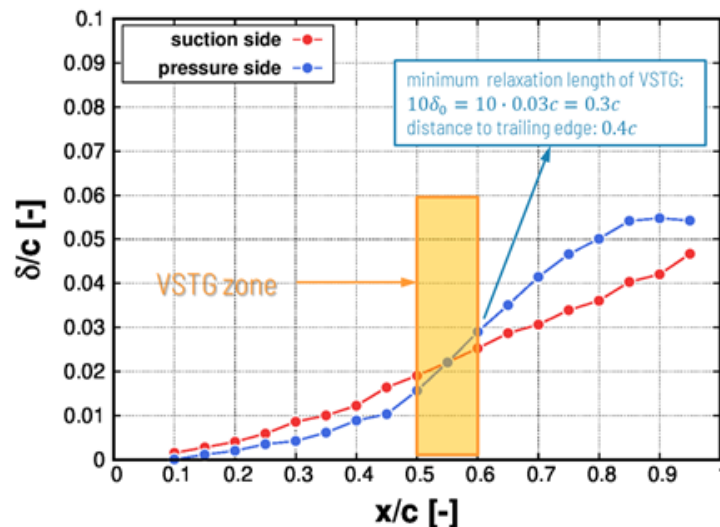

Fig. 12   Analysis of boundary layer thickness (δ) distribution from presursor RANS simulation of Upstream CFD to determine VSTG location for zonal scale-resolving simulations.

A preliminary analysis was also performed by UCFD to determine a suitable location for the VSTG zones on both airfoil sides, which was then adopted in the WRD simulation. For this purpose, the boundary layer thickness distribution of the precursor RANS was analysis again (see figure 12). Although the VSTG method is based on physical principles and uses the RANS boundary layer solution as input for its modelling, the structures initially generated in the volume source region are never fully physically accurate, and require a certain relaxation length downstream of the VSTG zone to become fully-developed. Previous studies for the VSTG method [26] suggest that about 10 boundary layer lengths are required to obtain a fully-developed flow profile. This means that the VSTG zones (both on the pressure as well as on the suction side) have to be placed far enough upstream of the trailing edge, so that the turbulence is fully-developed when it reaches this crucial region. The VSTG zones were therefore placed between $0.5 \leq x/c \leq 0.6$. The boundary layer thickness at $x/c = 0.6$ is roughly $0.03c$ on both airfoil sides, so that a relaxation length of 10δ would result in a full adaption of the flow until $x/c = 0.9$.

In all scale-resolving simulations, a time step size of $\Delta t \sim 0.001 \times c/U_\infty$ was prescribed (see table 2), which guarantees that the criterion $\mathrm{CFL_{max}} \leq 1$ is adhered to in all regions featuring resolved turbulence on all partner grids. UCFD simulated a time sample of $T_{\mathrm{sim}} = 42.5 \times c/U_\infty$, from which the first $10.6 \times c/U_\infty$ of initial transient were discarded from the statistical analysis. In the WRD simulation, statistics were collected over a slightly smaller time interval of $24 \times c/U_\infty$, with an additional simulation time of $8 \times c/U_\infty$ deemed to be initial transient.

C. Aeroacoustics post-processing

Aeroacoustic control surfaces of different sizes and types are evaluated by the two partners, where the control surfaces used in the simulations of Upstream CFD are shown in figure 13. Two main strategies are hereby assessed, which both employ sampling of unsteady flow data and subsequent farfield sound extrapolation via the Ffowcs Williams-Hawkings equation (FWH) [27]. The first strategy pursued by both partners and denoted as "Curle" accounts only for noise sources originating from solid surfaces, in this case simply the entire airfoil surface, and ignoring volume-source terms in the FW-H equation (this follows Curle's theory [28] of dipole sound sources on solid surfaces). The second strategy only explored by Upstream CFD uses permeable surfaces enclosing the turbulent acoustic source region, and is labelled "FWH" (as the full FWH equations are evaluated in this case). The main motivation for pursuing both the Curle and FWH strategies is to verify whether potential quadrupole sources inside the volume region can be traced in the simulation, which could indicate unwanted spurious noise sources originating either from the applied numerics or meshing strategy. Following Curle's theory, dipole sound from the solid surfaces should dominate in the low Mach number regime, so that strong physical quadrupole sources are not anticipated at the simulated Mach number of ~ 0.2. This assessment is supported by the measured farfield spectra, which exhibit a 5th power Mach number scaling that is characteristic for non-compact dipole sources (see figure 7). In the vicinity of the airfoil, the permeable control surface engulfs the airfoil at a distance of $0.25c$. The control surface then stretches to $5.0c$ downstream of the trailing edge, and exhibits a lateral extent of $0.8c$ at the most downstream location. The opening angles of the FWH surface were adjusted to the wake topology, and are thus specific to the simulated angle of attack $\alpha = 6°$. No closing surface is used at the downstream end, which invalidates the sound prediction for the very shallow farfield angles pointing in this direction. However, this also eliminates the need to implement complex averaging techniques for the treatment of the closing plane (e.g. the windowing procedure of Freund [29]). The current methodology with open FWH surface has been successfully validated in the past by Fuchs et al. [30]. For the acoustic post-processing of the WRD simulation, the FW-H solver ACCO developed at IAG was employed to calculate the farfield pressure at prescribed observer positions. The ACCO code has been widely used in combination with FLOWer, in particular for rotary wing applications [31] [32], since the implemented formulation can take moving sources into account. Parallel execution of the utility enables fast processing times for large numbers of time samples and observer locations. Unsteady simulation data is extracted from the solid and permeable control surfaces in the simulations of Upstream CFD at every 5th time step, which results in a maximum frequency resolution of $f_{\mathrm{max,FWH}} = 10$ kHz (based on the Nyquist) or a maximum Strouhal number of $St_{\mathrm{max,FWH}} \sim 4.9 \times U_\infty/d_{\mathrm{TE}}$ (based on the trailing edge thickness). WRD used a 2.5 times higher sampling rate in their simulation, resulting in a maximum resolved Strouhal number of $St_{\mathrm{max,FWH}} \sim 12.25 \times U_\infty/d_{\mathrm{TE}}$. In this case, only data for solid FWH control surfaces was extracted from the simulation.
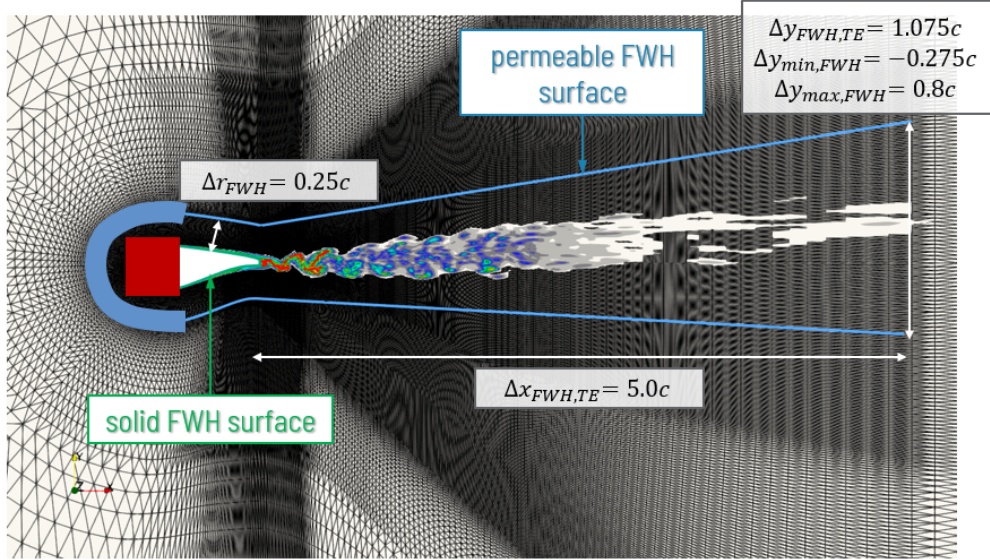
Fig. 13 Aeroacoustic post-processing strategy of Upstream CFD (the triangulated appearance of the mesh is a visualisation artefact).

Different scaling laws were applied to the resulting farfield sound pressure levels from CFD to normalise the data with regard to different parameters:

$$\text{PSD}_{\text{norm}} = \text{PSD}_{\text{CFD}} + 10 \cdot \log_{10}\left(L_{\text{span,ref}}/L_{\text{span,CFD}}\right) + 20 \cdot \log_{10}\left(d_{\text{CFD}}/d_{\text{ref}}\right) + 50 \cdot \log_{10}\left(M_{\text{ref}}/M_{\text{CFD}}\right) . \quad (1)$$

All data was scaled to a reference span width of $L_{\text{span,ref}} = 1$ m (corresponding to the span width for which the microphone array data in the experimental campaign was evaluated), which results in a correction of +7.5 dB for the CFD spectra. A reference observer distance of $d_{\text{ref}} = 1$ m relative to the trailing edge was assumed in all CFD post-processing as well as in the normalisation procedure applied for the experimental data. A 5th power scaling with Mach number was assumed, which is consistent with the sound scaling observed in the experimental campaign (see figure 7). The chosen reference Mach number used for the rescaling was set to the measured Mach number in the aeroacoustical test, i.e. $M_{\text{ref}} = 0.2$. The sound pressure levels resulting from the UCFD simulations were hence corrected by −0.37 dB due to the difference in freestream Mach number (see table 1).

V. Results

A. Assessment of DDES-specific shielding function

A precursor investigation was conducted by Upstream CFD to assess the behaviour of the DDES-specific shielding function in the non-zonal simulation methodology, which is a critical aspect of many hybrid RANS/LES turbulence models. Ideally, the shielding function should enforce RANS mode operation in the attached boundary layers on the suction and pressure sides up to the separation points in the trailing edge region in this simulation scenario. For this purpose, the DDES standard formulation [15] was compared to the more recently published formulation of Deck & Renard [16]. Selected plots of this limited study are presented in figure 14.

It became clear that severe shielding issues (i.e. significant drop in wall shear stress and premature flow separation) were encountered when employing the standard formulation on the non-zonal grid of UCFD. A critical quantity to assess for this analysis is the ratio between local grid resolution and boundary layer thickness, which is plotted in figure 14 (where the boundary layer thickness was extracted from a precursor RANS). Although no generally applicable threshold value exists (the case-by-case behaviour often depends on peculiarities of the local flow such as pressure gradients), shielding issues commonly start to arise for values of $\Delta/\delta \sim 0.1 - 0.3$, as reported e.g. in [15] and [16].

standard shielding function of Spalart et al. [15]   **shielding function of Deck & Renard [16]**
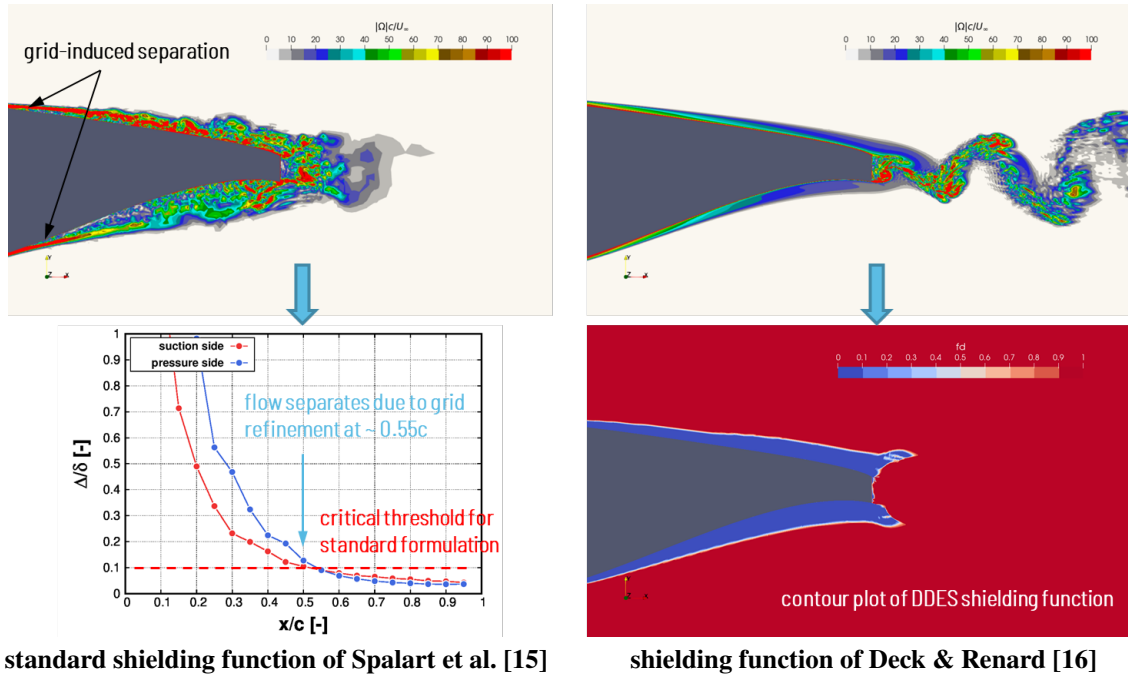
Fig. 14   Analysis of different formulations for DDES-specific shielding function: Preliminary simulation on test grid with standard formulation and SA-σ-DDES model (left), simulation on productive grid with enhanced shielding protection (right).

As the boundary thickness steadily grows downstream of the leading edge, it becomes more and more likely that the stated threshold value for the given shielding criterion will be reached. For the utilised non-zonal grid of UCFD, a value of $\Delta/\delta \sim 0.1$ is reached at $x/c \sim 0$, even though this particular is grid is not specifically refined in this region. From figure 14, that this leads to flow separation occurring on both suction and pressure sides in the simulation with the standard shielding function formulation (triggered by a decline in wall shear stresses). This illustrates that an a priori analysis based on e.g. a RANS solution can indeed be helpful in foreseeing possible shielding problems for the standard formulation. To find a solution which does not involve manually adapted grid coarsening, the more recently published shielding formulation of Deck & Renard [16] was assessed in conjunction with the SA-σ-DDES model. This test proved to be highly successful. The novel shielding function was able to fully protect the RANS boundary layers on both sides of the airfoil, and retracted rapidly downstream of the trailing edge where the simulation switches to scale-resolving LES mode (see figure 14). It was therefore decided to employ the new shielding function in all non-zonal simulations of UCFD. For all zonal simulations by both partners, using the enhanced shielding formulation is not beneficial, since RANS mode operation is fixed up until the start of the two VSTG zones (i.e. for $x/c < 0.5$). For $x/c > 0.5$, the applied turbulence models switch into WMLES mode, for which a shielding formulation that retreats in the upper part of the boundary layer is desired. This is not the operation mode for which the formulation of Deck & Renard was devised, which aims to shield the entire attached boundary layer (it was not tested whether the shielding function of Deck & Renard would fully re-build downstream of a VSTG region, or whether a residual LES region would persist in the upper part of the boundary layer). However, for the WMLES simulations, both partner opted to use established blending functions for this scenario, i.e the IDDES blending function in case of WRD and the standard DDES blending function in conjunction with the σ-DDES used by UCFD.

B. Assessment of performance of volumetric synthetic turbulence generator

One of the crucial aspects of the zonal setups used by both UCFD and WRD is the correct functionality and efficiency of the volumetric turbulence generator, which is used to inject resolved structures into the attached boundary layers on both sides of the airfoil. In figure 15, the distributions of the surface friction coefficient as well as standard deviation of surface pressure are shown for all conducted scale-resolving simulations.
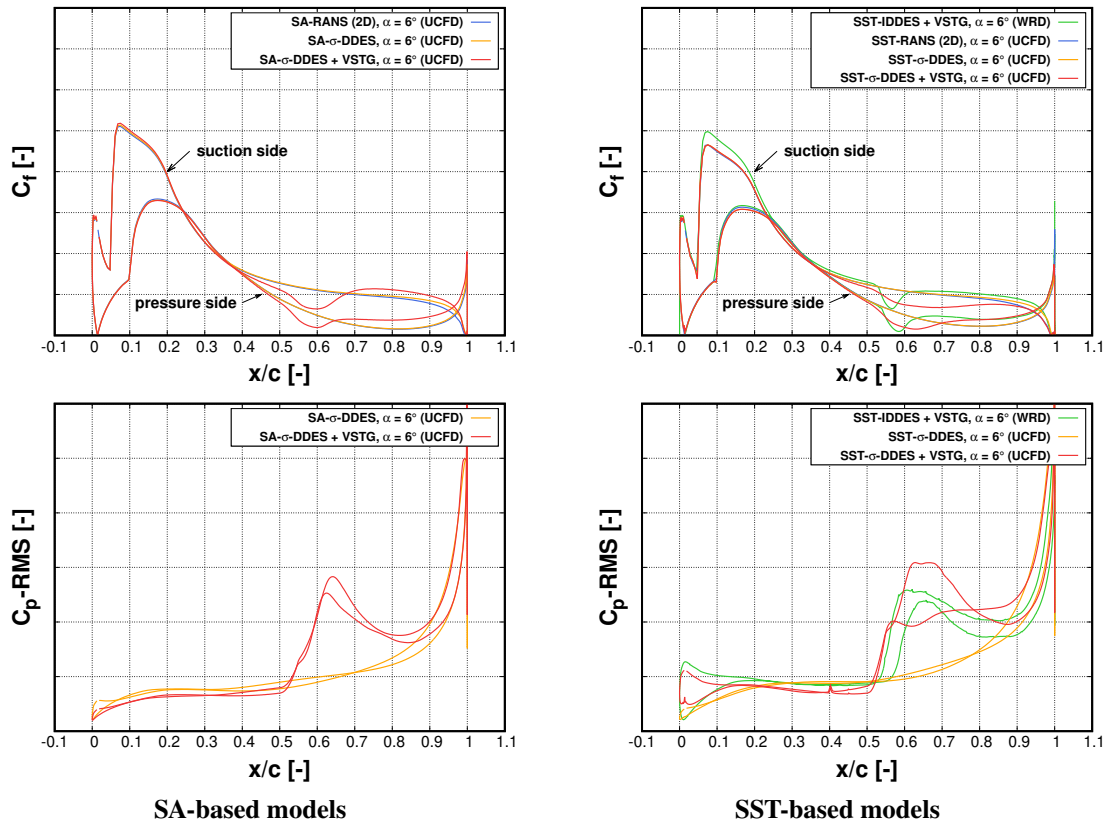

Fig. 15   Comparison of skin friction coefficient and standard deviation of the surface pressure coefficient between all CFD simulations.

Surface friction is also plotted for 2D RANS for reference. It can be seen that the manual tripping at 5% chord suction side and 10% chord pressure side applied in all CFD simulations seems to work consistently in both codes. Unfortunately, no experimental reference data is available for this quantity, so that a detailed assessment of how well the manual tripping applied in the CFD reproduces the influence of the tripping devices used in the measurements (see figure 3) could not be conducted. A slight difference in the predicted wall friction between the SST-IDDES simulation of WRD and the SST-based simulations of UCFD is observed near the suction peak around the leading edge. For $x/c < 0.5$, all scale-resolving models should still be in RANS mode, where RANS mode operation is even explicitly enforced in this region in all zonal simulations. For the σ-DDES simulations, the same wall friction profiles are returned as in the 2D RANS calculations. We therefore suspect that the differences in C_f originate from particular implementation details of the underlying SST model in both codes. However, no detailed comparison of the implemented equations, terms and model constants was conducted, so this issue could not be fully clarified yet. As detailed in section IV.B, the volumetric source terms of the VSTG method are active in the region $0.5 \leq x/c \leq 0.6$ in all partner simulations (see also figure 12). It can be seen that the inclusion of the VSTG region leads to an initial drop off of wall shear stress levels in all zonal simulations relative to the reference 2D RANS and the non-zonal σ-DDES simulations without VSTG (which return very similar C_f as the 2D RANS except close to the trailing edge). In general, the relaxation length that is required for the wall friction to recover appears to be comparable on both airfoil sides. This seems to be consistent with the fact that

the boundary layer thickness is very similar on both airfoil sides in the region $0.5 \leq x/c \leq 0.6$ (see figure 12), and that the grid resolution was manually adapted to the estimated boundary layer thickness by each partner. In line with expectation, the additional refinement applied in the WRD grid in the WMLES region leads to a much shorter recovery region in their simulation compared to the zonal simulations of UCFD, in which the boundary layer resolution was approximately 3 times coarser (see table 2). The difference is especially pronounced on the suction side of the profile, where less geometry curvature and flow acceleration is present in the region $0.5 \leq x/c \leq 1.0$ than on the pressure side. When comparing the performance of the VSTG between SA- and SST-based scale-resolving simulations of UCFD, it can be seen that the C_f recovery is somewhat more gradual in case of the SST-based σ-DDES model. In addition, the base value of C_f downstream of the recovery region seems to be a bit higher for all zonal simulations compared to the non-zonal simulations, especially on the pressure side.

C. Validation of aerodynamics prediction

Validation is first presented for the aerodynamics prediction of the scale-resolving CFD approaches, before acoustic results are discussed in sections V.D and V.E. In figure 16, time-averaged surface pressure coefficients from all CFD simulations are compared to the experimental measurements from both the closed and open test sections of the NWB wind tunnel. In general, the scale-resolving simulations reproduce the experimental surface pressure distribution well, which was somewhat expected due to the low angle of attack that was simulated ($\alpha = 6°$ still falls within the linear regime of the lift curve, and is considerably lower than the angle of attack with maximum lift for this profile). In fact, both 2D RANS simulations show even slightly better agreement in C_p than all DES-based simulations. Furthermore, no significant influence with regard to the choice of the RANS background model seems to be present. The most pronounced differences can be seen near the suction peak at the airfoil leading edge and around the airfoil trailing edge region, where all DES slightly tend towards the measurements with free transition ("clean") rather than the reference test with applied tripping. We suspect that cancellation-of-errors might play a role here, since the simple manual approach used for the tripping in the CFD probably does not reproduce fully the effect of the tape in the experiment. An interesting observation can be made in the VSTG region, where the activity of the VSTG source terms appear to lead to a noticeable kink in the C_p-distribution between $0.53 < x/c < 0.62$, which is especially pronounced in the WRD simulation. This seems to correspond with the sharper drop off of C_f noticed on the much more refined WRD grid (see figure 15). A less pronounced kink is also seen in the C_p-distribution of the SA-σ-DDES simulation with VSTG of UCFD, which is again consistent with the trend seen in the C_f-distribution compared to SST-σ-DDES with VSTG run, in which the decline in skin friction is more gradual.

A comparison of the CFD data with the wake rake measurements conducted is presented in figure 17 (no rake measurements were performed in the open wind tunnel test). The lateral flow profiles were extracted in the near wake region at a streamwise location $0.5c$ downstream of the trailing edge. Experimental reference data is available here in the form of static and total pressure coefficients. All DES is seen to agree generally well with the rake measurements, where the width of the wake is reasonably well predicted by the scale-resolving simulations. However, the total pressure drop is slightly over-predicted by all SRS compared to the tripped experiment, but agrees quite well with the test with free transition. In contrast, both 2D RANS models fail completely in predicting the static pressure drop in the wake as well as significantly under-predict the lateral extent of the wake. Moreover, the peak total pressure drop is significant over-predicted. However, the integrated total pressure loss of the wake is comparable to the DES simulations due to the erroneous compensation from the under-predicted wake width. This highlights the reliability issue of (steady-state) RANS predictions for complex wake flows, where the wake topology is often inaccurately captured, but cancellation-of-errors can lead to a false sense of trustworthiness in the eyes of the CFD user (especially if only integral quantities are inspected). With regard to the level of turbulence that is resolved in the wake region, a comparison between resolved kinetic energy profiles is additionally plotted in figure 17. Here, the turbulence levels in the WRD simulation are slightly lower than in the UCFD simulations.

In addition to mean flow quantities, spectral solution content from the scale-resolving CFD is compared with unsteady surface pressure measurements from the fiber optic sensors, where spectra for streamwise positions of $x/c = 0.86$ and 0.935 on both the suction and pressure side are shown in figure 18. All power spectral densities are normalised to a flow Mach number of 0.2 using 5th power scaling and plotted in dB (with $p_{\text{ref}} = 2 \times 10^{-5}$ Pa). It can be seen that both non-zonal and embedded approaches of UCFD and WRD capture the dominant tone which originates from the trailing edge shedding reasonably well. For the closed rig wind tunnel test, the dominant shedding frequency

observed in the surface pressure probes is roughly $f \sim 390$ Hz, which corresponds to a Strouhal number of $St \sim 0.182$ based on the trailing edge thickness. The shedding frequency in the open test rig campaign is somewhat lower, where values of $f \sim 320$ Hz or $St \sim 0.168$ were measured. In the WRD simulation, the observed shedding frequency of $St \sim 0.18$ corresponds closer to the data from the closed test section, whereas all UCFD simulations feature Strouhal numbers of $St \sim 0.172$, which is more aligned with the open test section data. However, possible differences seen in the comparison might also arise from the somewhat coarse frequency resolution of the CFD spectra, i.e. $\Delta St \approx 0.01$. With regard to the predicted broadband levels, the two non-zonal SRS simulations of UCFD clearly underestimate PSD levels by more than 10 dB at the four sensor locations shown in figure 18, as the incoming boundary layers are completely void of resolved turbulence. In contrast, the three zonal simulations of UCFD and WRD seem to capture the broadband levels reasonably well. The largest differences between measurements and CFD are seen for the sensor location at $x/c = 0.935$ on the pressure side, where broadband levels are underestimated by 2-4 dB in the zonal simulations. It is not entirely clear why this particular location on the pressure side seems to be more challenging to predict than others, since the spectra at the upstream location of $x/c = 0.86$ correspond reasonably well between experiments and CFD, both in spectral shape and in observed PSD broadband levels.
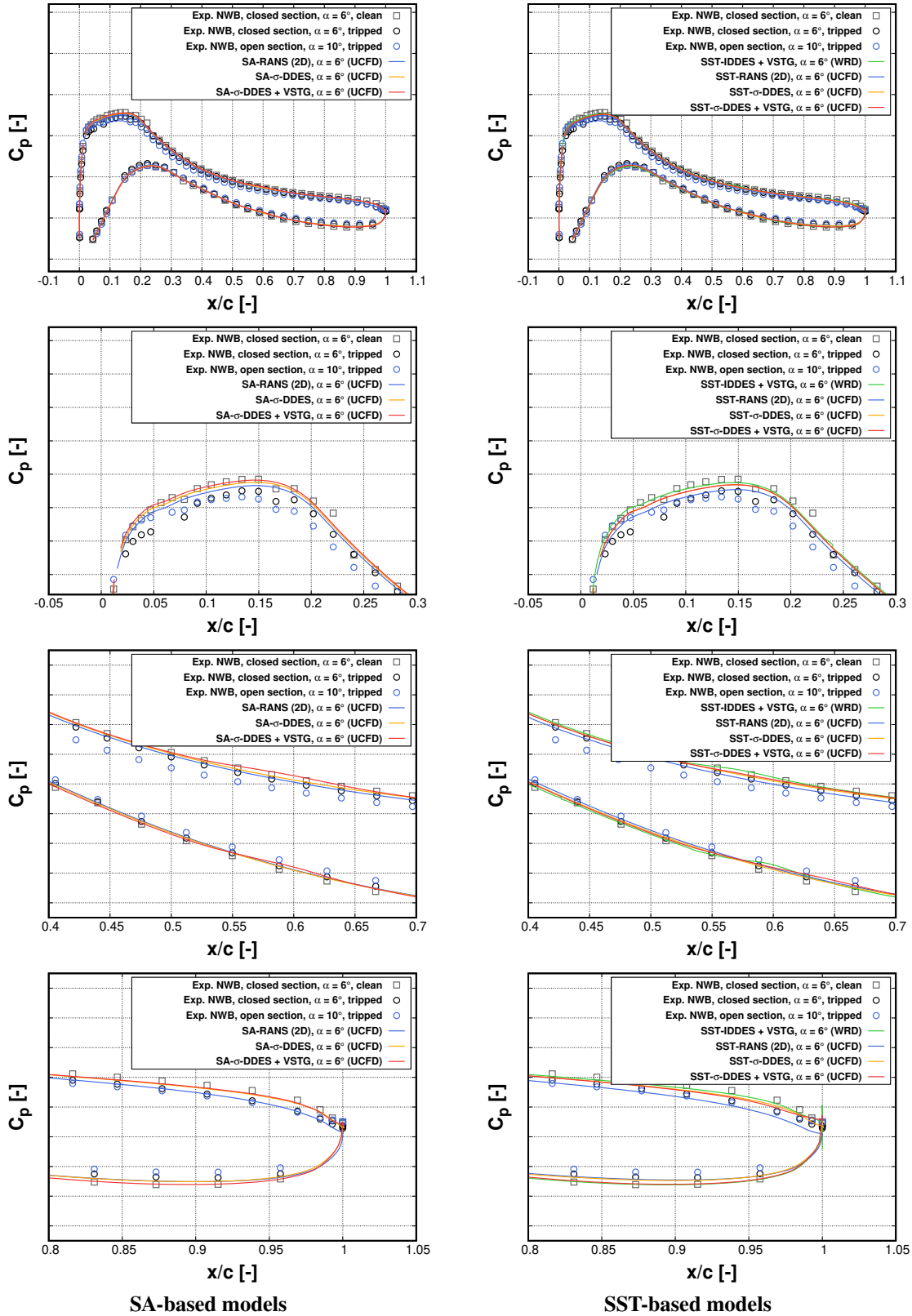
Fig. 16   Comparison of mean surface pressure coefficient between experimental measurements and CFD data. Magnified views of different regions are presented, i.e. the leading edge region on the suction side, the region in which the VSTG is applied and the trailing edge region.
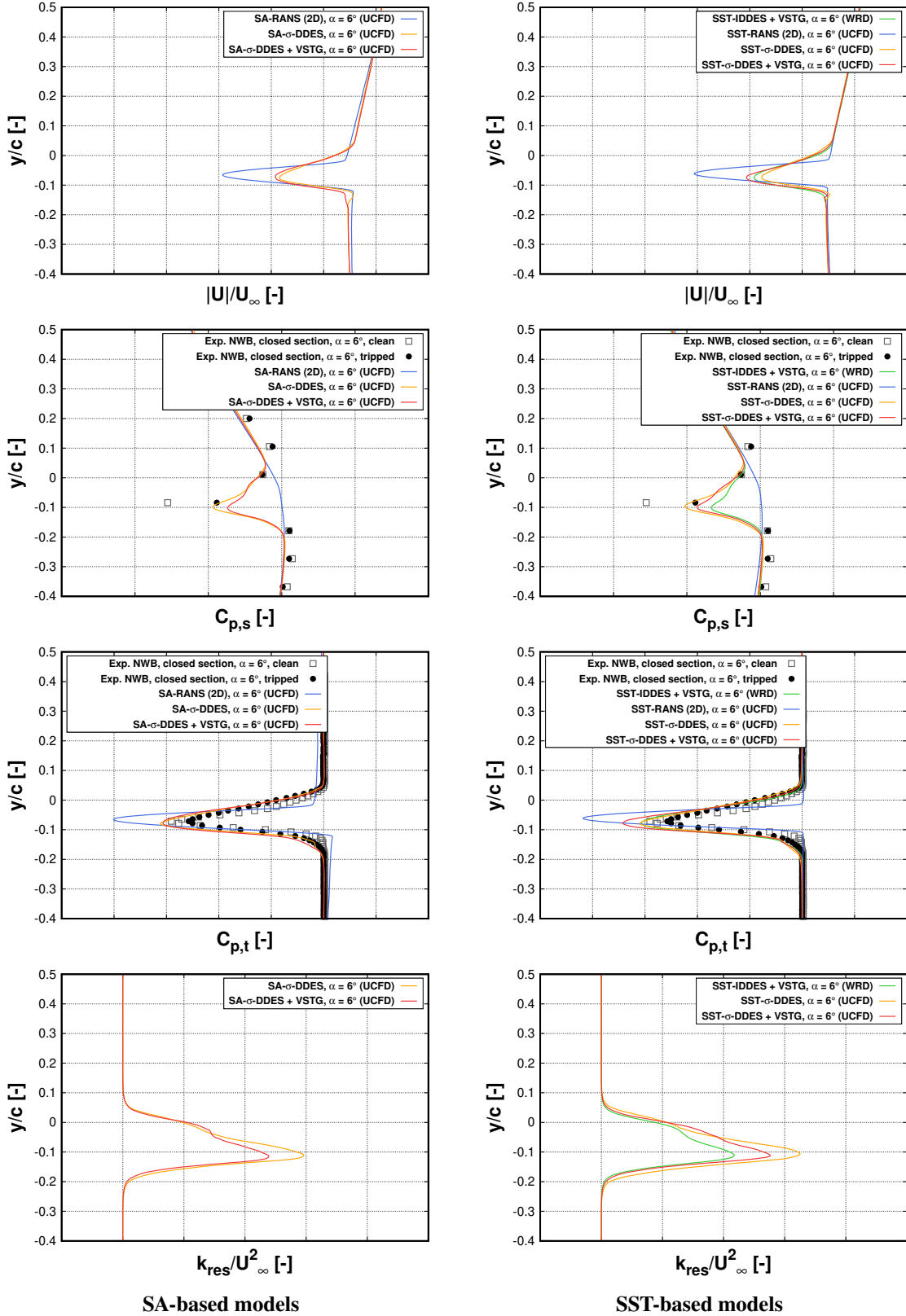
Fig. 17 Comparison of different lateral flow profiles between rake measurements and CFD at section $0.5c$ downstream of trailing edge. Plotted flow quantities: normalised velocity magnitude, static pressure coefficient $C_{p,s}$, total pressure coefficient $C_{p,t}$, resolved kinetic energy from CFD.
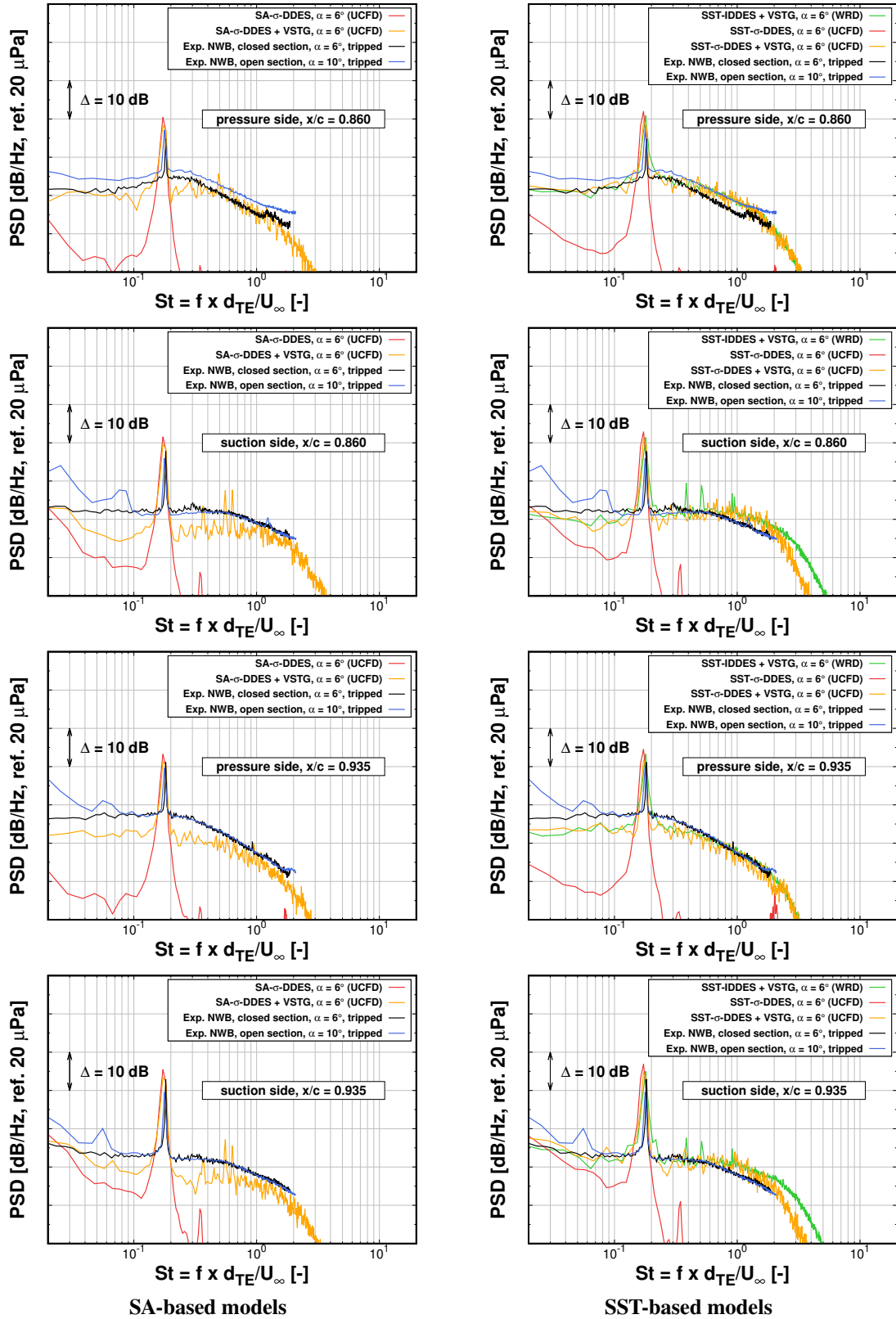
Fig. 18 Comparison of surface pressure spectra from fiber optic sensors and scale-resolving simulations of both partners. All spectra normalised to a reference Mach number of 0.2.

D. Assessment of quality of predicted farfield sound from solid and permeable FWH control surfaces

As detailed in section IV.C, Upstream CFD implemented both solid as well as permeable FWH surfaces in their setup. At the simulated Mach number of 0.219 and based on the assumption that boundary layer trailing edge noise dominates (i.e. dipole noise sources near the trailing egde), we would expect that both methods yield a comparable farfield sound prediction, since no significant quadrupole effect should be present. However, previous studies from the authors [30] as well as other groups [33] showed that discrepancies between solid and permeable FWH sound prediction can occur even at these Mach numbers in aeroacoustics simulations, and can potentially be associated with spurious noise sources, which can strongly depend on the particular choice of discretisation methods or scheme settings. In case of the cited publications, a rudimentary landing gear was investigated at a freestream Mach number of $M_\infty = 0.12$. We hence consider comparing sound predictions from solid and permeable FWH surfaces an important test for validating the reliability of an aeroacoustics tool chain for such applications.

SA-σ-DDES + VSTG
standard hybrid scheme settings

SST-σ-DDES + VSTG
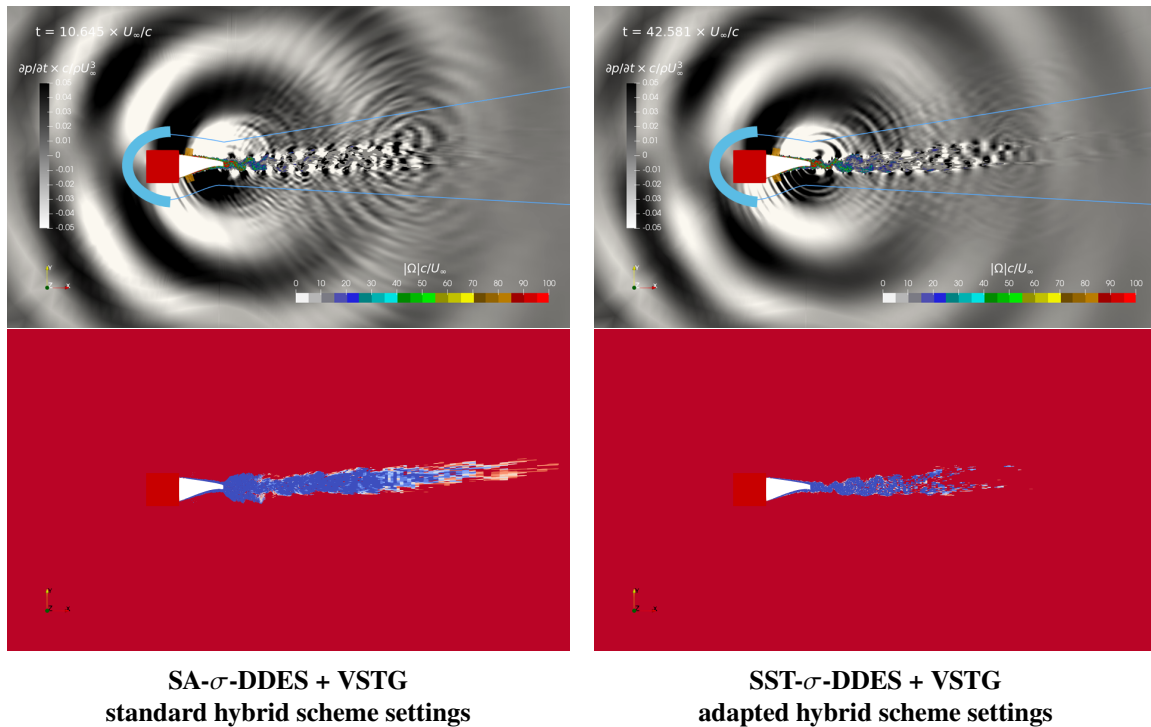**adapted hybrid scheme settings**

Fig. 19   Influence of numerical scheme settings in simulations of Upstream CFD on spurious noise emission in far wake region. Contours of pressure time derivation $\partial p/\partial t$ normalised by $\rho_\infty U_\infty^3/c$ as well as clipped contours of vorticity magnitude $|\Omega|$ normalised by U_∞/c (top). Permeable FWH surface is marked in blue. Contour of sensor function ζ of employed hybrid convection scheme (bottom). Upwind-biased scheme active in red regions, central differencing scheme is active in blue regions.

In figure 19, instantaneous acoustic fields visualised via the time derivative of the pressure field are shown for the two SRS simulations of UCFD which employed the VSTG method. The scaling of $\partial p/\partial t$ was adjusted to reflect a meaningful acoustic range, with the hydrodynamic fluctuations in the wake being fully saturated. Resulting farfield spectra in the form of power spectral densities scaled to dB from all four UCFD simulations are shown in figure 20. Here, predicted sound from both the Curle approximation (i.e. the solid airfoil surface) as well as the permeable FWH surface are shown. Multiple observations can be deduced from the two figures. Firstly, strong low-frequent acoustic waves are present in both flow fields, which emanate from the airfoil trailing edge and represent the dominant shedding tone found in all farfield spectra at $f \sim 355$ Hz. Accordingly, the second harmonic of the shedding tone can be found in all spectra at the doubled frequency of $f \sim 710$ Hz. Unfortunately, strong spurious noise can also be identified in the SA-based simulations, which appears to emanate from a region approximately between $1 \leq x/c \leq 3$ downstream of

the trailing edge. The strong acoustic waves generated in this region of the wake are not only visible in the acoustic field visualisation, but lead to a significant pile-up of acoustic energy in the mid-frequency range of the farfield spectra (centred around $f \sim 1.8$ kHz). Since the permeable control surface stretches to $5c$ downstream of the trailing edge, the spurious waves are "detected" by the FWH formulation, a significant difference between the prediction from the solid and the permeable FWH surfaces arises in the frequency range 1 kHz $\leq f \leq 2.6$ kHz. This is especially pronounced for the non-zonal SA-σ-DDES simulation, where sound levels of the permeable FWH surface are up by ~ 15 dB at $f \sim 1.8$ kHz relative to the Curle surface.
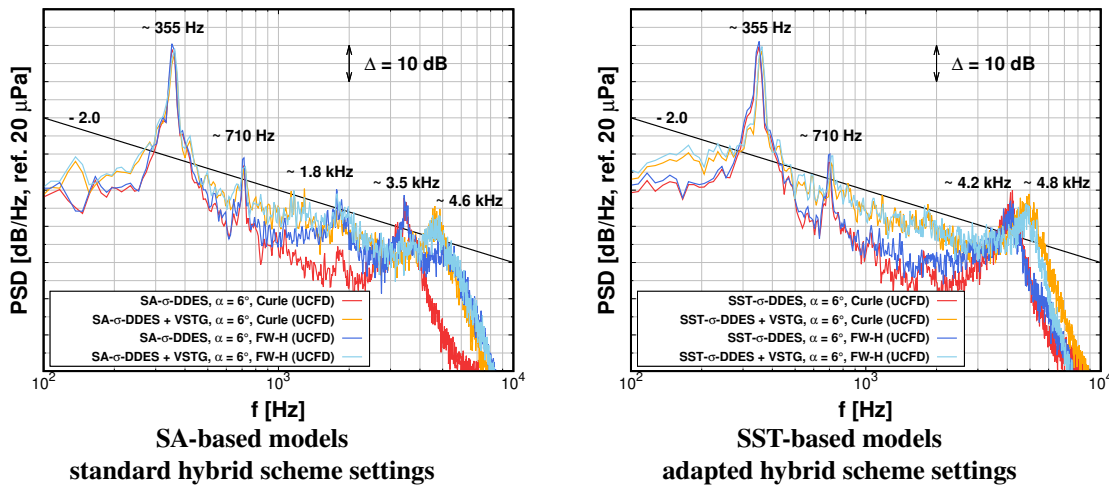

Fig. 20 Influence of numerical scheme settings in simulations of Upstream CFD on predicted farfield sound spectra. All spectra are normalised to an observer distance of 1 m and a spanwidth of $S = 1$ m. The farfield radiation angle is $\theta \approx 96.2°$, pointing towards the airfoil suction side (i.e. upwards in the positive y-direction).

A detailed analysis was performed by Upstream CFD to understand the causes for this behaviour. One of the main contributing factor that could be identified is the apparent sensitivity of the applied hybrid blending convection scheme towards certain scheme settings. As introduced in section III.A, Upstream CFD employs the hybrid convection scheme of Travin et al. [12] in their scale-resolving simulations, which blends seamlessly between an upwind-biased scheme in the irrotational flow region and a central differencing scheme in the turbulence-resolving region based on a flow-dependent sensor function ($\zeta_{min} = 0 \leq \zeta \leq \zeta_{max} = 1$). This particular blending scheme has been successfully utilised by different groups of the hybrid RANS-LES community [34] [35] since its publication in 2004 and generally offers the advantage of providing low-dissipative numerics inside the scale-resolving region whilst maintaining numerical stability in the farfield / irrotatioal regions. In addition, the user does not have to prescribe the blending regions in a zonal manner, since the sensor function automatically evaluates the blending behaviour locally. However, this leads to a situation in which the hybrid scheme has to blend between the two schemes at some downstream location inside the wake region, as vorticity (to which the sensor function is sensitised) declines steadily towards the farfield and the turbulent structures start to dissipate. Usually, a blending between 2nd order accurate central differences ($\zeta = 0$) and a 2nd order accurate upwind scheme ($\zeta = 1$) is employed by UCFD, which was found to deliver very accurate results for a range of flows [18]. However, this particular application was found to be very sensitive to specific settings of the hybrid convection scheme, at least with regard to the farfield sound prediction. This situation is probably exaberated by the fact that no significant natural noise sources are present in the wake region, so that any spurious noise is not disguised by physical noise but plainly exposed. Before the SST-based scale-resolving simulations, a confined parameter study was conducted by Upstream CFD to optimise the settings of the hybrid scheme for this particular test case. It was found that lowering the ζ_{max} parameter of the scheme and thus allowing some of the central differencing discretisation to be mixed into the upwind-biased discretisation in the irrotational region provides a smoother blending for the fading turbulent structures in the wake region. This measure alone lead to a significant reduction of spurious noise, as can be seen in the $\partial p/\partial t$ contour plot in figure 19 for the SST-σ-DDES simulation with VSTG. Both SST-based scale-resolving simulations of

UCFD were thus conducted with the adapted hybrid scheme settings, which leads to a much more consistent prediction between solid and permeable FWH surfaces (see figure 20). Particularly in the frequency range 1 kHz $\leq f \leq$ 2.6 kHz, which was strongly affected by spurious noise in the SA-based simulations, PSD levels from both FWH methods now show a much better agreement. In addition to the spurious noise sources in the wake region, another acoustical artefact was identified in all simulations. High-frequent waves are seen to emanate from the trailing edge region, and are also featured in the acoustic farfield spectra in form of a characteristic bump centred around $f \sim 3.5 - 4.8$ kHz (where the frequency depends on the RANS background model and the simulation mode, see figure 20). We suspect that this non-physical artefact originates from the shear layer roll-up at the trailing edge, and is a common feature sometimes observed in scale-resolving simulations. No direct measures were explored in this study to mitigate this issue. However, the affected frequencies are relatively high, and thus of lesser practical importance.
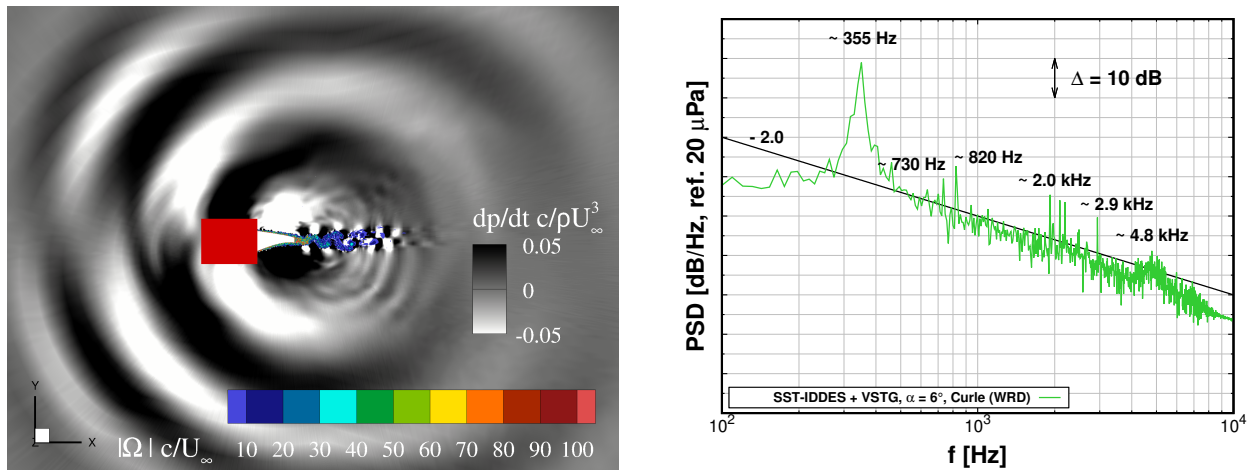

Fig. 21 **Instantaneous acoustical field of WRD simulation employing SST-IDDES and the VSTG method (left). Contours show pressure time derivation $\partial p/\partial t$ normalised by $\rho_\infty U_\infty^3/c$ as well as clipped contours of vorticity magnitude $|\Omega|$ normalised by U_∞/c. Farfield sound spectrum from WRD simulation (right). The farfield radiation angle is $\theta \approx 96.2°$, pointing towards the airfoil suction side (i.e. upwards in the positive y-direction).**

An equivalent analysis of the simulated farfield sound was conducted for the SST-IDDES simulation of WRD, where results are presented in figure 21. In line with the scale-resolving simulations of UCFD, the dominant shedding tone is prominently featured in the simulation of WRD at approximately the same frequency of 355 Hz. A high-frequent hump centred around $\sim$ 4.8 kHz can also be noted in the computed farfield spectrum, although it is less pronounced than in the UCFD data (peak PSD level is roughly 10 dB lower). However, additional artefacts are present, which are not featured in the UCFD spectra. Close to the peak of the second harmonic, a second peak at $f \sim 820$ Hz is present in the mid-frequency range. Further additional peaks can be detected at higher frequencies (three peaks clustered around 2 kHz and one at approximately 2.9 kHz). Unfortunately, farfield sound could only be post-processed from solid surfaces by WRD, so that a comparison to permeable FWH data is not available for this simulation. However, additional high-frequent waves are visible in the contour plot of the acoustic field, which seem to emanate from the near wake region. Their wave number appears to be about 5 times lower than the wave number of the shedding tone, which translates into a frequency of $f \sim 1.8$ kHz. An investigation into the origin of this tone is ongoing, and can potentially be clarified in future publications.

E. Validation of farfield sound prediction

For the validation of the farfield sound prediction of the conducted CFD simulations, measured data from the experimental microphone array is used, which represents farfield levels emanating from a mid-span section of the airfoil with a span width of 1 m (see section II). The measurements of the reference (freefield) microphone could not be used in this context, since they include additional spurious noise sources from the test rig and are thus not representative for the broadband levels of the airfoil in freefield conditions. As detailed in section II, the microphone array was mounted on the suction side of the airfoil and presents a farfield observer angle of $\theta \approx 96°$ relative to the freesteam velocity vector and the trailing edge. A comparison between farfield sound from CFD and the experimental array data in the form of power spectral density levels is shown in figure 22.
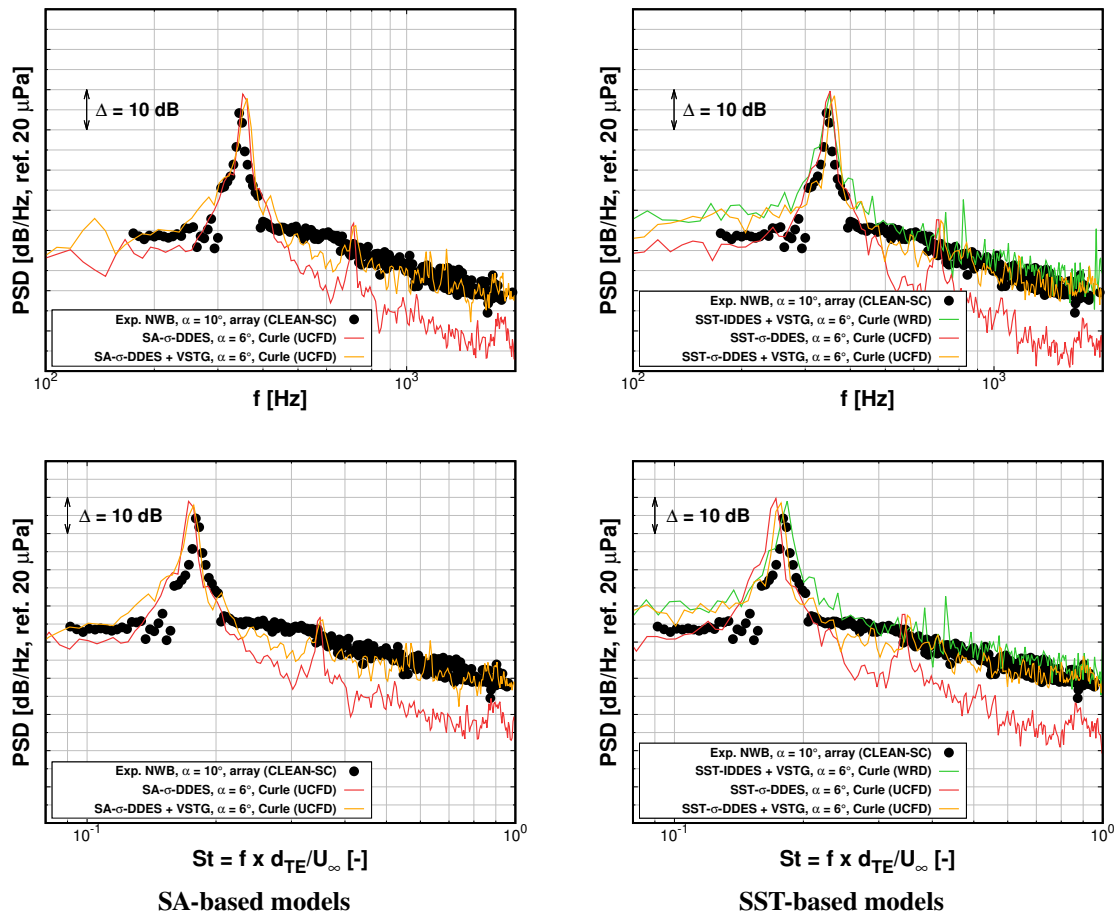

Fig. 22 **Comparison of farfield sound results from microphone array measurements and scale-resolving simulations of Upstream CFD and WRD. All spectra are normalised to an observer distance of** 1 m**, a spanwidth of** $S = 1$ m **and a Mach number of** $M = 0.2$**. The farfield radiation angle is** $\theta \approx 96.2°$**, pointing towards the airfoil suction side (i.e. upwards in the positive** y**-direction).**

Scaling is shown for both the native frequency range in Hz as well as the normalised Strouhal number based on the trailing edge thickness, where the shown range was adapted to the valid frequency range of the experimental data set. Only solid FWH results from CFD are presented here to allow for direct comparability. However, permeable FWH results of UCFD were already presented in figure 20, and are very similar to the solid results of UCFD in the plotted frequency range (except for the non-zonal SA-σ-DDES simulation, for which the spurious wake noise leads to significant differences between solid and permeable FWH predictions for $f > 1$ kHz). In general, all scale-resolving CFD is seen to capture the dominant tonal component well, both in level and frequency. When normalised to Strouhal

26

number, the tonal components in the UCFD ($St \sim 0.174$) and WRD ($St \sim 0.186$) simulations are slightly shifted relative to measured value of $St \sim 0.18$. These values are also consistent with the dominant shedding frequency observed in the hydrodynamic pressure spectra near the trailing edge (see figure 18). With regard to the prediction of the broadband sound levels, it can be seen that better agreement to the experimental data is achieved with the zonal / embedded approach, where both non-zonal simulations under-estimate broadband levels significantly by more than 10 dB in the mid-frequency range (i.e. 500 Hz $< f <$ 2 kHz). Slightly higher broadband levels ($\sim$ 1-2 dB, dependent on the frequency) are featured in the SST-IDDES simulation of WRD compared to the zonal SST-σ-DDES simulation of UCFD. However, the same broadband level scaling trend of f^{-2} is seen in both simulations, which is consistent with the scaling observed in the experiment (compare with figure 7).

VI. Conclusions and outlook

Overall, the ambitious goals set at the outset of this study have been widely achieved. A comprehensive experimental campaign was conducted in both a closed and an open test section of the NWB wind tunnel, where extensive flow field and acoustic measurements were obtained. Excellent comparability could be achieved between the aerodynamic performance of the airfoil mock-up in both tests, so that a consistent, high-quality reference data set for the validation of different CFD approaches could be obtained (both in terms of aerodynamics and noise). Different scale-resolving CFD methods and models were assessed by both partners in a blind study, with no a prior knowledge of the experimental results. In general, excellent agreement could be achieved between CFD and experiment. Both investigated DES variants, i.e. the SST-IDDES and the σ-DDES models, deliver very similar results when applied in conjunction with the VSTG method. This indicates that for the embedded approach used in this work, the grey-area extension of the σ-DDES model is not vital for an accurate flow and sound prediction, which we tentatively anticipated before the beginning of this study. However, the fact that the σ-DDES model can be reliably applied in both non-zonal and zonal simulation methodologies is an achievement in itself, and suggests that the IDDES variant as a dedicated WMLES method can potentially be abandoned in the future. The shielding problems reported for the standard DDES formulation highlight the need for more research in this vital area, since the current formulation seems to fail under too many practical conditions. However, further studies are required to assess the reliability of the new approach of Deck & Renard [16] that was initially evaluated in this work. For the embedded hybrid RANS-LES approach with synthetic turbulence, this is less of an issue, since the RANS and LES zones were fixed a priori.

Future work will focus on refining the current numerical methodologies of WRD and UCFD, and in particular on exploring new strategies to further minimise spurious noise sources in the simulations. The application seems to be particularly susceptible to spurious noise from different sources, since physically generated broadband levels are relatively low. With regard to the experimental data, further post-processing will be conducted for the directional microphone data, so that these measurements can also be used for validation purposes in the future.

Acknowledgments

References

[1] Jackson, K., Zuteck, M., van Dam, C., Standish, K., and Berry, D., "Innovative design approaches for large wind turbine blades," *Wind Energy*, Vol. 8, No. 2, 2005, pp. 141–171. https://doi.org/10.1002/we.128.

[2] Standish, K., and van Dam, C., "Aerodynamic analysis of blunt trailing edge airfoils," *Journal of Solar Energy Engineering*, Vol. 125, No. 4, 2003, pp. 479–487.

[3] Stone, C., Barone, M., Smith, M., and Lynch, E., "A computational study of the aerodynamics and aeroacoustics of a flatback airfoil using hybrid RANS-LES," *47th AIAA Aerospace Sciences Meeting including The New Horizons Forum and Aerospace Exposition, Orlando, FL, AIAA 2009-273*, 2009.

[4] Papadakis, G., and Manolesos, M., "The flow past a flatback airfoil with flow control devices: Benchmarking numerical simulations against wind tunnel data," *Wind Energy Science*, Vol. 5, No. 3, 2020, pp. 911–927.

[5] Bergmann, A., "The aeroacoustic wind tunnel DNW-NWB," *In: Proceedings of the 18th AIAA/CEAS Aeroacoustics Conference, Colorado Springs, CO, AIAA 2012-2173*, 2012. https://doi.org/10.2514/6.2012-2173.

[6] Sijtsma, P., "CLEAN based on spatial source coherence," *International Journal of Aeroacoustics*, Vol. 6, No. 4, 2007, pp. 357–374.

[7] Schlinker, R., "Airfoil Trailing Edge Noise Measurements with a Directional Microphone," *4th Aeroacoustics Conference*, American Institute of Aeronautics and Astronautics, Atlanta, GA, U.S.A., 1977. https://doi.org/10.2514/6.1977-1269.

[8] Sen, R., "Interpretation of Acoustic Source Maps Made with an Elliptic-Mirror Directional Microphone System," *Aeroacoustics Conference*, American Institute of Aeronautics and Astronautics, State College,PA,U.S.A., 1996. https://doi.org/10.2514/6.1996-1712.

[9] Brooks, T., Pope, D., and Marcolini, M., "Airfoil Self-Noise and Prediction," Tech. Rep. NASA Reference Publication 1218, 1989.

[10] Brooks, T., and Hodgson, T., "Trailing Edge Noise Prediction from Measured Surface Pressures," *Journal of Sound and Vibration*, Vol. 78, No. 1, 1981, pp. 69–117. https://doi.org/10.1016/S0022-460X(81)80158-7.

[11] Knacke, T., "Potential effects of Rhie & Chow type interpolations in airframe noise simulations," *Accurate and efficient aeroacoustic prediction approaches for airframe noise*, edited by C. Schram, R. Dénos, and E. Lecomte, VKI lecture notes, Von Kármán Institute for Fluid Dynamics, Rhode-Saint-Genèse, Belgium, 2013.

[12] Travin, A., Shur, M., Strelets, M., and Spalart, P., "Physical and numerical upgrades in the detached-eddy simulation of complex turbulent flows," *Advances in LES of complex flows*, 2004, pp. 239–254.

[13] Mockett, C., Fuchs, M., Garbaruk, A., Shur, M., Spalart, P., Strelets, M., Thiele, F., and Travin, A., "Two non-zonal approaches to accelerate RANS to LES transition of free shear layers in DES," *Progress in Hybrid RANS-LES Modelling, Notes on Numerical Fluid Mechanics and Multidisciplinary Design*, Vol. 130, edited by S. Girimaji, W. Haase, S.-H. Peng, and D. Schwamborn, Springer, Heidelberg, 2015, pp. 187–201.

[14] Fuchs, M., Mockett, C., Sesterhenn, J., and Thiele, F., "The grey-area improved σ-DDES approach: Formulation review and application to complex test cases," *Progress in Hybrid RANS-LES Modelling, Notes on Numerical Fluid Mechanics and Multidisciplinary Design*, Vol. 143, edited by Y. Hoarau, S.-H. Peng, D. Schwamborn, A. Revell, and C. Mockett, Springer, 2020, pp. 119–130.

[15] Spalart, P., Deck, S., Shur, M., Squires, K., Strelets, M., and Travin, A., "A new version of detached-eddy simulation, resistant to ambiguous grid densities," *Theoretical and Computational Fluid Dynamics*, Vol. 20, No. 3, 2006, pp. 181–195.

[16] Deck, S., and Renard, N., "Towards an enhanced protection of attached boundary layers in hybrid RANS/LES methods," *Journal of Computational Physics*, Vol. 400, 2020, p. 108970.

[17] Shur, M., Strelets, M., and Travin, A., "Acoustically-adapted versions of STG," *Go4Hybrid: Grey Area Mitigation for RANS-LES Methods - Results of the 7th Framework Research Project Go4Hybrid, Funded by the European Union, 2013-2015*, edited by C. Mockett, W. Haase, and D. Schwamborn, Notes on Numerical Fluid Mechanics and Multidisciplinary Design, Springer International Publishing AG, 2017, Chap. 2.2.2.

[18] Fuchs, M., Mockett, C., Sesterhenn, J., and Thiele, F., "Recent results with Grey-Area improved DDES for a wide range of flows," *Progress in Hybrid RANS-LES Modelling, Notes on Numerical Fluid Mechanics and Multidisciplinary Design*, Vol. 137, edited by Y. Hoarau, S.-H. Peng, D. Schwamborn, and A. Revell, Springer, 2018, pp. 195–206.

[19] Kroll, N., Eisfeld, B., and Bleecke, H., "FLOWer," *Notes on Numerical Fluid Mechanics*, Vol. 71, 1999, pp. 58–68.

[20] Jameson, A., Schmidt, W., and Turkel, E., "Numerical solution of the Euler equations by finite volume methods using Runge Kutta time stepping schemes," *AIAA Journal*, , No. 81, 1981, p. 1259.

[21] Jameson, A., "Time dependent calculations using multigrid, with applications to unsteady flows past airfoils and wings," *10th Computational Fluid Dynamics Conference*, 1991, p. 1596.

[22] Shur, M., Spalart, P., Strelets, M., and Travin, A., "A hybrid RANS-LES approach with delayed-DES and wall-modelled LES capabilities," *International Journal of Heat and Fluid Flow*, Vol. 29, No. 6, 2008, pp. 1638–1649.

[23] Metzinger, C., Chow, R., Baker, J., Cooperman, A., and Van Dam, C., "Experimental and computational investigation of blunt trailing-edge airfoils with splitter plates," *AIAA Journal*, Vol. 56, No. 8, 2018, pp. 3229–3239.

[24] Garbaruk, A., Leicher, S., Mockett, C., Spalart, P., Strelets, M., and Thiele, F., "Evaluation of Time Sample and Span Size Effects in DES of Nominally 2D Airfoils beyond Stall," *Progress in Hybrid RANS-LES Modelling, Notes on Numerical Fluid Mechanics and Multidisciplinary Design*, Vol. 107, edited by W. Schröder, Springer, 2010, pp. 87–99.

[25] Menter, F., "Best practice: scale-resolving simulations in ANSYS CFD," Tech. Rep. 2.00, ANSYS Germany GmbH, November 2015.

[26] Mockett, C., Haase, W., and Schwamborn, D., *Go4Hybrid: Grey Area Mitigation for RANS-LES Methods - Results of the 7th Framework Research Project Go4Hybrid, Funded by the European Union, 2013-2015*, Notes on Numerical Fluid Mechanics and Multidisciplinary Design, Vol. 134, Springer International Publishing AG, 2017.

[27] Farassat, F., "Derivation of Formulations 1 and 1A of Farassat," *NASA Technical Memorandum 214853*, March 2007.

[28] Curle, N., "The influence of solid boundaries upon aerodynamic sound," *Proceedings of the Royal Society of London, Series A*, Vol. 231, 1955, pp. 505–514.

[29] Freund, J., "Noise sources in a low-Reynolds-number turbulent jet at Mach 0.9," *Journal of Fluid Mechanics*, Vol. 438, 2001, pp. 277–305.

[30] Fuchs, M., D., F., Mockett, C., Kramer, F., Knacke, T., Sesterhenn, J., and Thiele, F., "Assessment of different meshing strategies for low Mach number noise prediction of a rudimentary landing gear," *In: Proceedings of the 23rd AIAA/CEAS Aeroacoustics Conference, AIAA AVIATION Forum, Denver, Co, AIAA 2017-3020*, 2017. https://doi.org/https://doi.org/10.2514/6.2017-3020.

[31] Kowarsch, U., Öhrle, C., Keßler, M., and Krämer, E., "Aeroacoustic simulation of a complete H145 helicopter in descent flight," *Journal of the American Helicopter Society*, Vol. 61, No. 4, 2016, pp. 1–13.

[32] Klein, L., Gude, J., Wenz, F., Lutz, T., and Krämer, E., "Advanced computational fluid dynamics (CFD)–multi-body simulation (MBS) coupling to assess low-frequency emissions from wind turbines," *Wind Energy Science*, Vol. 3, No. 2, 2018, pp. 713–728.

[33] Spalart, P., Shur, M., Strelets, M., and Travin, A., "Sensitivity of landing-gear noise predictions by large-eddy simulation to numerics and resolution," *50th AIAA Aerospace Sciences Meeting Including the New Horizons Forum and Aerospace Exposition*, 2012, p. 1174.

[34] Mockett, C., Perrin, R., Reimann, T., Braza, M., and Thiele, F., "Analysis of detached-eddy simulation for the flow around a circular cylinder with reference to PIV data," *Flow, turbulence and combustion*, Vol. 85, No. 2, 2010, pp. 167–180.

[35] Menter, F., and Egorov, Y., "SAS turbulence modelling of technical flows," *Direct and Large-Eddy Simulation VI*, Springer, 2006, pp. 687–694.